



PII S0016-7037(02)00909-2

Chemical and isotopic constraints on the generation and transport of magma beneath the East Pacific Rise

K. W. W. SIMS,^{1,2} S. J. GOLDSTEIN,^{2,*} J. Blichert-Toft,³ M. R. PERFIT,⁴ P. KELEMEN,¹ D. J. FORNARI,¹ P. MICHAEL,⁵ M. T. MURRELL,² S. R. HART,¹ D. J. DEPAOLO,⁶ G. LAYNE,¹ L. BALL M. JULL¹ and J. BENDER⁷

¹Department of Geology and Geophysics, Woods Hole Oceanographic Institution, Woods Hole, MA 02543, USA

²Los Alamos National Laboratory, Los Alamos, NM 87545, USA

³Ecole Normale Supérieure, Lyon, France

⁴Department of Geological Sciences, University of Florida, Gainesville, FL 32611-2120, USA

⁵Department of Geosciences, University of Tulsa, Tulsa, OK 74104, USA

⁶Berkeley Center for Isotope Geochemistry, University of California, Berkeley, Berkeley, CA 94720, USA

⁷Department of Geography and Earth Sciences, University of North Carolina, Charlotte, NC 28223, USA

(Received April 26, 2001; accepted in revised form March 22, 2002)

Abstract—Interpretation of U-series disequilibria in midocean ridge basalts is highly dependent on the bulk partition coefficients for U and Th and therefore the mineralogy of the mantle source. Distinguishing between the effect of melting processes and variable source compositions on measured disequilibria (^{238}U - ^{230}Th - ^{226}Ra and ^{235}U - ^{231}Pa) requires measurement of the radiogenic isotopes Hf, Nd, Sr, and Pb. Here, we report measurements of ^{238}U - ^{230}Th - ^{226}Ra and ^{235}U - ^{231}Pa disequilibria; Hf, Nd, Sr, and Pb isotopic; and major and trace element compositions for a suite of 20 young midocean ridge basalts from the East Pacific Rise axis between 9°28' and 9°52'N. All of the samples were collected within the axial summit trough using the submersible Alvin. The geological setting and observational data collected during sampling operations indicate that all the rocks are likely to have been erupted from 1991 to 1992 or within a few decades of that time. In these samples, ^{230}Th excesses and ^{226}Ra excesses are variable and inversely correlated. Because the eruption ages of the samples are much less than the half-life of ^{226}Ra , this inverse correlation between ^{230}Th and ^{226}Ra excesses can be considered a primary feature of these lavas. For the lava suite analyzed in this study, ^{226}Ra and ^{230}Th excesses also vary with lava composition: ^{226}Ra excesses are negatively correlated with Na_8 and La/Yb and positively correlated with $\text{Mg}\#$. Conversely, ^{230}Th excesses are positively correlated with Na_8 and La/Yb and negatively correlated with $\text{Mg}\#$. Th/U , $^{230}\text{Th}/^{232}\text{Th}$, and ^{230}Th excesses are also variable and correlated to one another. ^{231}Pa excesses are large but relatively constant and independent of $\text{Mg}\#$, La/Yb , Th/U , and Na_8 . The isotope ratios $^{143}\text{Nd}/^{144}\text{Nd}$, $^{176}\text{Hf}/^{177}\text{Hf}$, $^{87}\text{Sr}/^{86}\text{Sr}$, and $^{208}\text{Pb}/^{206}\text{Pb}$ are constant within analytical uncertainty, indicating that they were derived from a common source. The source is homogeneous with respect to parent/daughter ratios Lu/Hf , Sm/Nd , Rb/Sr , and Th/U ; therefore, the measured variations of Th/U , ^{230}Th , and ^{226}Ra excesses and major and trace element compositions in these samples are best explained by polybaric melting of a homogeneous source, not by mixing of compositionally distinct sources. Copyright © 2002 Elsevier Science Ltd

1. INTRODUCTION

Measurement of U-series disequilibria in young midocean ridge basalts (MORBs) should, in principle, provide unique constraints on the mechanisms and time scales of melt generation and transport. U-series isotopes have now been measured in several MORB suites by mass spectrometric methods (Goldstein et al., 1989, 1992, 1993, 1994; Volpe and Goldstein, 1993; Lundstrom et al., 1995, 1998, 1999; Sims et al., 1995; Bourdon et al., 1996), and a number of models relating U-series disequilibria to melting process have been proposed (e.g., McKenzie, 1985; Williams and Gill, 1989; Qin, 1992; Iwamori, 1993, 1994; Spiegelman and Elliott, 1993; Richardson and McKenzie, 1994).

However, interpretation of the MORB U-series data in terms of melting processes has been limited by uncertainties in eruption age, magma storage times, and mantle source composition. Until now, most MORB suites measured for U-series disequi-

libria were collected by dredging, resulting in large uncertainties in inferred sample eruption age. As a result, it is uncertain whether the ^{226}Ra excesses in these suites are primary or have been modified by decay, given that the half-life of ^{226}Ra is 1600 yr. Therefore, the presence of ^{226}Ra excesses has been used simply as an indication that samples are less than a few thousand years old. This has been useful in interpreting data on ^{230}Th and ^{231}Pa excesses, which have much longer half-lives (75,380 and 32,760 yr, respectively).

Furthermore, very few MORB samples measured for U-series have also been analyzed for radiogenic isotopes of long-lived parents. In the few cases in which both types of data are available, Nd and Sr isotope data indicate that the sample suites measured for U-series isotopes are derived from heterogeneous sources (Ben Othman and Allegre, 1990; Ruben and MacDougall, 1992; Sims et al., 1995). Creation of U-series disequilibria in basalts during melting is dependent on the bulk partition coefficients for U and Th and, therefore, the mineralogy of the mantle source. As a result, uncertainties or variability in the source composition make it difficult to determine the extent to which variations in U-series excesses reflect variations in melt-

* Author to whom correspondence should be addressed (ksims@whoi.edu).

ing processes vs. variations in the source lithology (e.g., garnet pyroxenite, garnet peridotite, spinel peridotite).

Application of U-Th-Ra and U-Pa radioactive disequilibria measurements to the study of MORB petrogenesis requires constraints on source composition and estimates of eruption age and magma storage time, relative to the half-lives of ^{230}Th , ^{231}Pa , and ^{226}Ra . Here, we report U-series disequilibria, radiogenic isotopic compositions (Nd, Sr, Hf, and Pb), and major and trace element compositions in a suite of 20 axial MORB samples from $9^{\circ}28'$ to $9^{\circ}52'\text{N}$ along the East Pacific Rise (EPR). These samples were collected by submersible (Haymon et al., 1993; Perfit et al., 1994; Fornari et al., 1998), and therefore, their geology, locations, and young ages are relatively well established. Furthermore, the ages of several of these samples have been determined using Po-Pb disequilibria (Rubin et al., 1994). Knowledge of the eruption ages for the axial samples eliminates a large uncertainty in the interpretation of the U-series measurements in this area. Constraints on mantle source composition from the Sr, Nd, Hf, and Pb isotope data enable us to distinguish between the effects of source variability and melting processes. Using the major and trace element compositions of these samples, we evaluate the time scales of magmatic differentiation and the influences of crustal residence on the U-series measurements (this is particularly critical for ^{226}Ra , which has a half-life of 1600 yr). We then use the compositions of these samples to evaluate melt generation and transport processes beneath the EPR.

In addition, we have measured the Nd, Sr, Hf, and Pb isotopic compositions of four samples from the Siqueiros Transform, $8^{\circ}20'\text{N}$ along the EPR, adjacent to the segment at 9 to 10°N . These samples have previously been measured for major and trace elements (Perfit et al., 1992) and U-Th-Ra and U-Pa disequilibria (Lundstrom et al., 1999). The Siqueiros MORB samples range from trace element depleted to trace element enriched and cover almost the entire range of U-Th-Ra disequilibria observed in MORBs. Determining the isotopic compositions of these samples is critical for interpretation of their U-series disequilibria. Comparison of these samples with the axial samples at 9 to 10°N enables us to evaluate the relative influence of variable source composition vs. variability in melt generation and transport processes beneath the EPR over a much larger range of U-Th-Ra disequilibria.

2. SAMPLE LOCATIONS, AGES, AND GEOLOGICAL SETTING

Sample locations and inferred ages are given in Table 1. All samples were collected within the Axial Summit Collapse Trough (ASCT) (Fornari et al., 1998) between $9^{\circ}28'$ and $9^{\circ}52'\text{N}$ along the EPR (Fig. 1) using the submersible *Alvin* during multiple cruises between 1991 and 1994. Ages (1991 to 1992) for some samples were established by Po-Pb dating (Rubin et al., 1994), while for others, there is extensive observational and geological evidence that suggests that lava ages are demonstrably younger (<200 yr) than the half-life of ^{226}Ra (Haymon et al., 1993; Perfit et al., 1994; Fornari et al., 1998).

The region of the EPR between $9^{\circ}28'$ and $9^{\circ}52'\text{N}$ is a fast-spreading ridge with a full spreading rate of 110 mm/yr (Fig. 1). Magnetic data indicate that the average spreading rate in this area has been constant over the past 2 Ma (Carbotte and

Macdonald, 1992). The continuity of the EPR axis is interrupted by a DEVAL at $9^{\circ}37'\text{N}$ (Langmuir et al., 1986), which has been shown to be a small overlapping spreading center (OSC) that acts as a hydrothermal and volcanological divide between the northern and southern ridge segments (Smith et al., 2001).

The axis north and south of this DEVAL has distinct morphologies that can be attributed to differences in tectonic and volcanic processes during the evolutionary history of each segment (Scheirer and Macdonald, 1993; Fornari et al., 1998). Bathymetry of the northern area near $9^{\circ}50'\text{N}$ shows it to be near the shallowest portion of the segment. It is characterized by a broad, smooth, and convex profile indicative of a more magmatically robust ridge segment (Scheirer and Macdonald, 1993). This area has a volcanically dominated, narrow axial trough usually <100 m wide and <15 m deep with sinuous walls created by collapse of the young lobate and sheet lava terrain. The EPR axis in the southern area near $9^{\circ}30'\text{N}$ is deeper and more triangular in profile, suggestive of a less robust magma supply. The axial trough near $9^{\circ}30'\text{N}$ is nearly 300 m wide and ~ 20 to 30 m deep with more linear walls and a nested inner trough. Observational data suggest that the recent magmatic input to the ridge segment north of $9^{\circ}37'\text{N}$ is representative of a longer term episode of enhanced magmatic activity on that section of ridge, relative to the region south of the OSC. Perfit and Chadwick (1998) and Fornari et al. (1998) suggest the older-looking, more evolved lavas and more tectonized morphology of the ASCT area around $9^{\circ}28'$ to $9^{\circ}34'\text{N}$ indicate that the axial segment south of the OSC at $9^{\circ}37'\text{N}$ has been, on average, less magmatic in recent times than the segment north of the OSC.

3. RESULTS

3.1. Major and Trace Elements

Major and trace element concentrations are reported in Appendix 1 together with details on analytical methods. All axial 9 to 10°N samples are tholeiitic, incompatible trace element depleted, "normal MORB" (N-MORB). Major element compositions range from relatively primitive to evolved (molar $\text{Mg}^{\#}$ ranges from 64 to 55), with the more evolved samples having higher concentrations of incompatible trace elements. The samples show limited variability in Mg-normalized Na content (Na_8 varies from 2.4 to 2.8) and incompatible trace element ratios, such as La/Yb, Sm/Nd, and U/Th. Trace element fractionations (e.g., Th/U and Sm/Nd) also vary with $\text{Mg}^{\#}$. Trace element ratios (e.g., U/Th and Sm/Nd) also vary with $\text{Mg}^{\#}$, especially for abundance data measured by isotope dilution mass spectrometry.

Samples from $9^{\circ}40'$ to $9^{\circ}52'\text{N}$ (henceforth distinguished as the $9^{\circ}50'\text{N}$ area) cover the entire range of major and trace element compositions seen in this area, with $\text{Mg}^{\#}$ varying from 58 to 66. The samples from $9^{\circ}28'$ to $9^{\circ}37'\text{N}$ (henceforth distinguished as the $9^{\circ}30'\text{N}$ area) are more evolved, as indicated by lower $\text{Mg}^{\#}$ values (range 58 to 60) and higher concentrations of incompatible trace elements. They may also have been derived from smaller degrees of partial melting, as indicated by higher Na_8 values and more fractionated incompatible trace element ratios.

Table 1. Sample locations, descriptions, and ages .

Sample	Long, west	Lat. north	Depth (m)	Description	Estimated age
9–10°N EPR					
2359-4	104°17.868'	9°53.274'	2558	Fresh lobate collapse, could be N end of 1991 flow	1991 flow or <10 yr
2497-1	104°17.848'	9°53.264'	2555	Young lobate lava in new rift that may have opened in late '91 or early '92	Late 1991 to 1992 flow, possibly unrelated to the 1991 flow to the south, Po-Pb dated
2359-5	104°17.874'	9°53.256'	2557	Older pillow in same area as 2359-4, slight Mn and sediment coating	10 to ~200 yr
2368-4	104°17.624'	9°50.927'	2522	Fresh ropy sheet flow from center of ASCT	1991 flow
2372-1	104°17.522'	9°50.601'	2521	East wall of ASCT, fresh young sheet flow (possible BBQ flow), basalt associated vent animals, and diffuse flow	1991 flow, Po-Pb dated
2392-9	104°17.520'	9°50.580'	2524	Ropy to hackley flow N of BBQ site, believed to be 1991 BBQ flow	1991 flow, Po-Pb dated
2752-6	104°17.478'	9°50.304'	2516	Fresh lobate-hackly flow on W side of ASCT, minor sediment and no Mn-coating on lava surface	1991 flow
2504-1	104°17.481'	9°50.303'	2515	Glassy flow on floor of ASCT	Late 1991 to 1992 flow, Po-Pb dated
2351-2	104°17.453'	9°50.139'	2514	Fresh glassy sheet flow near hydrothermal vent in ASCT	1991 flow
2746-4	104°17.293'	9°48.921'	2515	Young drained-out lobe near edge of ASCT, could be younger than 2746-3b or same as 1991 flow	Possible 1991 flow or <20 yr
2746-3b	104°17.244'	9°48.905'	2514	Young, glassy lobate lava with a thin dusting of sediment and Mn coating.	<20 yr
2370-6	104°17.160'	9°48.396'	2523	Top of E ASCT wall, serpulid worm attached, may be slightly older than 2370-1	<10 yr
2370-1	104°17.021'	9°47.546'	2523	Fresh glassy lobate flow from top of ASCT wall at edge of breakout, associated with bacterial mat	Possible 1991 flow
2355-8	104°16.620'	9°45.852'	2536	Fresh ropy flow on floor of ASCT, near bacterial floc site and diffuse hydrothermal venting	1991 flow
2356-7	104°15.925'	9°40.896'	2554	Fresh basalt, ropy to flat sheet from center of ASCT near shimmering water and bacteria	1991 flow
2361-6	104°15.628'	9°39.123'	2559	Lobate crust from top of east ASCT wall in slightly older looking area, with light sediment cover	<100 yr
2352-2	104°14.958'	9°33.444'	2565	Massive sheet to ropy flow from floor of ASCT, likely part of ODP flow	10 to 100 yr
2358-3	104°14.652'	9°30.876'	2574	Top of lobate flow at south margin of ODP flow, slightly stained/altered surface	10 to 100 yr
2358-4	104°14.652'	9°30.876'	2578	Massive ponded ODP flow, top is flat sheet flow surface	10 to 100 yr
2365-3	104°13.086'	9°16.794'	2584	Youngest flow in 9°17' area, curtain folded in collapse area (near F vent of Von Damm et al., 1996)	<10 yr
Siqueiros Transform					
2390-5	104°02.27'	8°18.36'		Mn-coated pillow basalt from the western RTI within the Siqueiros transform, area is older looking with moderate sediment cover	>8000 yr; 43,632 to 44,481 yr
D20-2	103°39.90'	8°22.21'		Young-looking pillow basalt fragment, very glassy and olivine rich with light coating of Fe-oxide, from same general area as dive 2384	<100 yr
2384-3	103°39.73'	8°22.25'		Glassy pillow lava from young-looking flows in relay zone between intratransform spreading centers A and B, sample is olivine rich with slight oxidized coating	<100 yr
2384-6	103°40.10'	8°22.26'		Glassy pillow lava from young-looking flows in relay zone between intratransform spreading centers A and B, sample is olivine rich with slight yellow/orange weathered surface	<100 yr

Sample ages estimated based on observational data collected using *Alvin* (Haymon et al., 1993; Perfit et al., 1994, 1996; Fornari et al., 1998). Ages ascribed to 1991 flow on the basis of Po-Pb dating (Rubin et al., 1994) and observations made in 1991 during or just following the eruption on the basis of pristine surface textures and patina of volcanic glass and location of samples within the axial trough. 1991 to 1992 flow age based on observation of lava issuing from fissures north of the BBQ site (Haymon et al., 1993). Other age estimates based on nearly a decade of observations at the 9°50'N East Pacific Rise area and comparisons made using video data and still photographs of lava surfaces proximal to fixed seafloor markers. Most locations are based on transponder navigation in *Alvin*. Navigation was not operative during dive 2361, so locations are based on *Alvin* positions determined from the surface ship using of global positioning system (GPS). Siqueiros sample locations are based on short-baseline trackpoint navigation of *Alvin* dives or, in the case of D20, estimates of dredge position based on the ships GPS location, wire out and wire angle. Age estimates for 2390-5 come from observational constraints (>8000 yr) and from model ages based upon U-Th (43,632 yr) and U-Pa disequilibria (44,481 yr) (see Lundstrom et al., 1999).

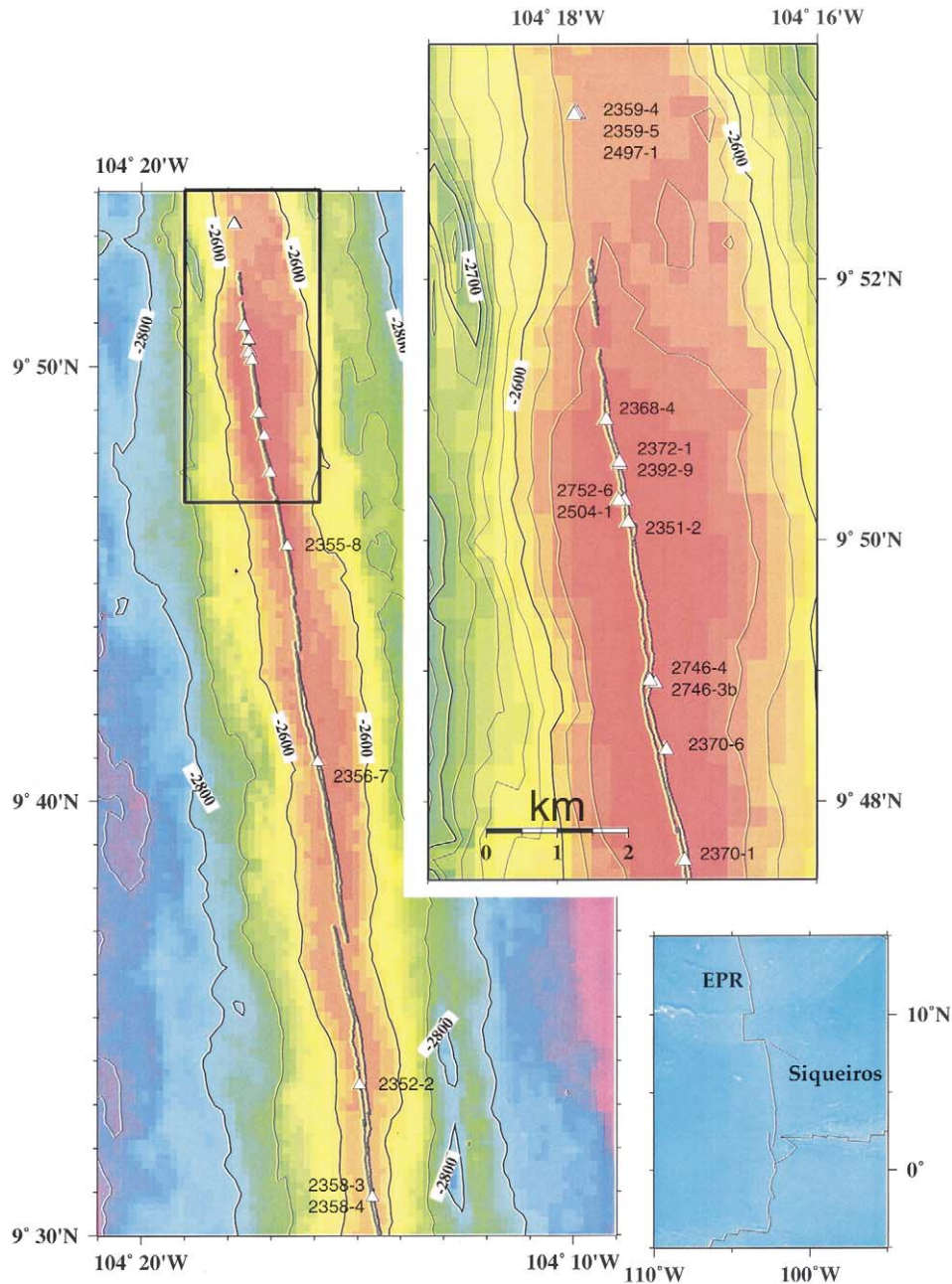


Fig. 1. Sample location maps. Lower right inset shows the East Pacific Rise (EPR) from 5°S to 15°N. Multibeam bathymetry (Cochran et al., 1999) shown in the two larger maps show the EPR axis between 9°30' and 9°50'N (left) and blow-up of the area near 9°50'N where most of the samples were collected by *Alvin*. Right map shows outline of the Axial Summit Collapse Trough (Fornari et al., 1998) with sample locations noted. Note DEVAL at 9°37'N along the EPR.

3.2. Radiogenic Isotopes: Nd, Sr, Hf, and Pb

Nd, Sr, Hf, and Pb isotopes for our axial 9 to 10°N samples are reported in Table 2 and shown in Figures 2 to 4. The Nd, Sr, and Hf isotopic compositions exhibit only slight differences and are essentially the same when compared to the Pacific MORB database ($^{143}\text{Nd}/^{144}\text{Nd}$ varies from 0.512378 ± 11 to 0.512400 ± 10 , $^{87}\text{Sr}/^{86}\text{Sr}$ varies from 0.70244 ± 5 to 0.70257 ± 6 , and $^{176}\text{Hf}/^{177}\text{Hf}$ varies from 0.283169 ± 5 to 0.283197 ± 5). The high-precision multiple-collector inductively coupled

plasma mass spectrometry (MC-ICP-MS) Pb data for $^{208}\text{Pb}/^{204}\text{Pb}$, $^{207}\text{Pb}/^{204}\text{Pb}$, and $^{206}\text{Pb}/^{204}\text{Pb}$ show small but significant variability; however, the $^{208}\text{Pb}/^{206}\text{Pb}$ isotopic ratios of these samples are nearly identical within analytical uncertainty (2.061 ± 1 to 2.065 ± 1).

3.3. U-Series Disequilibria Measurements

U, Th, Pa, and Ra concentrations and $^{234}\text{U}/^{238}\text{U}$, $^{230}\text{Th}/^{232}\text{Th}$, $^{230}\text{Th}/^{238}\text{U}$, $^{226}\text{Ra}/^{230}\text{Th}$, and $^{231}\text{Pa}/^{234}\text{U}$ for the axial 9

Table 2. Sr, Nd, Hf, and Pb isotopic compositions for the 9°N East Pacific Rise (EPR) and Siqueiros Transform samples.

Sample	⁸⁷ Sr/ ⁸⁶ Sr ^a	¹⁴³ Nd/ ¹⁴⁴ Nd ^b	ε _{Nd}	¹⁷⁶ Hf/ ¹⁷⁷ Hf ^c	ε _{Hf}	²⁰⁸ Pb/ ²⁰⁴ Pb ^d	²⁰⁷ Pb/ ²⁰⁴ Pb ^d	²⁰⁶ Pb/ ²⁰⁴ Pb ^d	²⁰⁸ Pb/ ²⁰⁶ Pb ^d
9 to 10°N EPR									
2359-4	0.70249 ± 5	0.512391 ± 8	10.9	0.283192 ± 5	14.9	37.651	15.459	18.250	2.063
2497-1(1)	0.70245 ± 4	0.512386 ± 9	10.8	0.283171 ± 7	14.1	37.656	15.472	18.248	2.064
2497-1(2)				0.283169 ± 5	14.0				
2359-5	0.70251 ± 4	0.512396 ± 8	11.0	0.283186 ± 5	14.6	37.655	15.454	18.260	2.062
2368-4	0.70246 ± 4	0.512400 ± 10	11.0	0.283189 ± 5	14.8	37.657	15.471	18.246	2.064
2372-1	0.70248 ± 4	0.512396 ± 6	11.0	0.283187 ± 6	14.7	37.661	15.470	18.247	2.064
2392-9	0.70253 ± 3	0.512395 ± 5	10.9	0.283195 ± 5	15.0	37.612	15.450	18.235	2.063
2752-6	0.70244 ± 5	0.512390 ± 8	10.8	0.283196 ± 5	15.0	37.743	15.494	18.313	2.061
2504-1	0.70245 ± 4	0.512386 ± 8	10.7	0.283197 ± 5	15.0	37.640	15.465	18.245	2.063
2351-2	0.70246 ± 4	0.512402 ± 5	11.1	0.283189 ± 5	14.8	37.673	15.472	18.260	2.063
2746-4	0.70244 ± 5	0.512400 ± 12	11.0	0.283190 ± 5	14.8	37.646	15.461	18.250	2.063
2746-3b	0.70249 ± 4	0.512378 ± 11	10.6	0.283184 ± 3	14.6	37.729	15.479	18.304	2.061
2370-6	0.70257 ± 6	0.512390 ± 7	10.8	0.283190 ± 4	14.8	37.732	15.489	18.299	2.062
2370-1	0.70250 ± 4	0.512396 ± 17	11.0	0.283186 ± 5	14.6	37.654	15.467	18.252	2.063
2355-8	0.70247 ± 4	0.512386 ± 10	10.7	0.283188 ± 4	14.7	37.679	15.480	18.258	2.064
2356-7	0.70249 ± 4	0.512392 ± 8	10.9	0.283193 ± 5	14.9	37.678	15.466	18.255	2.064
2361-6	0.70248 ± 5	0.512395 ± 6	10.9	0.283176 ± 5	14.3	37.750	15.487	18.284	2.065
2352-2	0.70249 ± 4	0.512404 ± 4	11.1	0.283189 ± 5	14.8	37.717	15.476	18.291	2.062
2358-3	0.70247 ± 5	0.512406 ± 5	11.1	0.283187 ± 5	14.7	37.743	15.488	18.299	2.063
2358-4	0.70247 ± 4	0.512407 ± 8	11.2	0.283177 ± 5	14.3	37.691	15.469	18.275	2.062
2365-3	0.70251 ± 4	0.512384 ± 7	10.7	0.283179 ± 5	14.4	37.693	15.470	18.271	2.063
Siqueiros									
2390-5	0.70294 ± 6	0.512241 ± 5	7.9	0.283035 ± 5	9.3	38.073	15.540	18.645	2.042
D20-2	0.70250 ± 4	0.512384 ± 5	10.7	0.283179 ± 7	14.4	37.861	15.498	18.355	2.063
2384-3	0.70255 ± 6	0.512387 ± 5	10.8	0.283194 ± 7	14.9	37.861	15.499	18.353	2.063
2384-6	0.70253 ± 6	0.512387 ± 7	10.8	0.283185 ± 6	14.6	37.814	15.487	18.316	2.065

^a Sr isotopes measured at Wood's Hole Oceanographic Institution by thermal ionization mass spectrometry (TIMS) using the VG 354. Uncertainties in measured Sr isotope ratios represent analytical errors ($2\sigma/\sqrt{n}$, where n is the number of measured ratios) reported in the last decimal place. Measured ratios are corrected to NBS 987 = 0.710240, measured every fifth sample. External reproducibility is 20 to 30 ppm based on replicate runs of NBS 987.

^b Nd isotopes measured at the University of California, Berkeley, by TIMS using the VG 354. Uncertainties in measured Nd isotope ratios are analytical errors ($2\sigma/\sqrt{n}$, where n is the number of measured ratios) reported in the last decimal place. Measured ratios are normalized to ¹⁴⁶Nd/¹⁴²Nd = 0.636151. Replicate measurement ($n = 71$) of ¹⁴³Nd/¹⁴⁴Nd in BCR-1 (between 10/02/92 and 4/04/01) gives a value of 0.511843 ± 5. ε_{Nd} values calculated using (¹⁴³Nd/¹⁴⁴Nd)_{Chur(0)} = 0.511836.

^c Hf isotopes measured at ENS Lyon by multiple collector inductively coupled plasma mass spectrometry (MC-ICP-MS) using the VG Plasma 54 (Blichert-Toft et al., 1997). Uncertainties in measured Hf isotope ratios are analytical errors ($2\sigma/\sqrt{n}$, where n is the number of measured ratios) reported in the last decimal place. Measured ratios are normalized for mass fractionation to ¹⁷⁹Hf/¹⁷⁷Hf = 0.7325. Measurement of ¹⁷⁴Hf/¹⁷⁷Hf in the JMC-475 Hf isotopic standard = 0.28216 ± 1. ε_{Hf} values calculated with (¹⁷⁶Hf/¹⁷⁷Hf)_{Chur(0)} = 0.28 2772.

^d Pb isotopes measured at ENS Lyon by MC-ICP-MS using the VG Plasma 54. Measured ratios are normalized to both an internal TI standard and then to NBS 981 using the values of Todt et al. (1996). For these measurements every two samples are interspersed with an analyses of NBS 960 for the mass bias correction (see White et al., 2000). Errors for ²⁰⁸Pb/²⁰⁴Pb, ²⁰⁷Pb/²⁰⁴Pb, and ²⁰⁶Pb/²⁰⁴Pb are 300 to 400 ppm (2σ) and for ²⁰⁸Pb/²⁰⁶Pb are 200 to 300 ppm (2σ) and are calculated by propagating [$\sqrt{(se^2 + se^2)}$] both the analytical error and the variance of the NBS 960 standards from the instrument fractionation trend observed during the sum of these analyses.

to 10°N samples are reported in Table 3 and shown in Figures 5 to 7. The ²³⁸U/²³²Th, ²³⁰Th/²³⁸U, ²³¹Pa/²³⁵U, and ²²⁶Ra/²³⁰Th measurements for samples 2392-9 and 2497-1b are consistent (within analytical uncertainties) with other thermal ionization mass spectrometry measurements (Lundstrom et al., 1999).

3.3.1. ²³⁸U-²³⁴U

All of the samples used in this study were fresh, hand-picked glasses and have ²³⁴U/²³⁸U activity ratios = 1 (±3‰), indicating minimal post-eruption alteration. For submarine basalts, ²³⁴U/²³⁸U activity ratios are a sensitive indicator of alteration, as seawater is significantly enriched in ²³⁴U relative to ²³⁸U (for seawater, ²³⁴U/²³⁸U = 1.14 ± 0.03) (Thurber, 1967; Ku et al., 1977).

3.3.2. ²³⁸U-²³⁰Th-²²⁶Ra

In all of the axial 9 to 10°N samples examined in this study, ²³⁰Th/²³⁸U is > 1 (Fig. 5), indicating that daughter ²³⁰Th has been enriched relative to its parent ²³⁸U (hereafter, ²³⁰Th/²³⁸U > 1 is referred to as ²³⁰Th excess). There is a correlation between Mg[#] and the extent of ²³⁰Th/²³⁸U disequilibrium: The more primitive samples show the smallest ²³⁰Th excesses, and the more evolved samples show progressively larger ²³⁰Th excesses (Fig. 8). ²³⁰Th excesses also increase with Mg-normalized Na contents and incompatible element fractionations such as La/Yb and Sm/Nd (Fig. 9).

²²⁶Ra/²³⁰Th is > 1 in all of the axial 9 to 10°N samples (Fig. 6), indicating that daughter ²²⁶Ra is enriched relative to parent ²³⁰Th (hereafter, ²²⁶Ra/²³⁰Th > 1 is referred to as ²²⁶Ra excess). There is an inverse correlation between Th excess and ²²⁶Ra excess: The samples with the lowest Th excess have the highest Ra excess and vice versa (Fig. 6A). ²²⁶Ra excesses

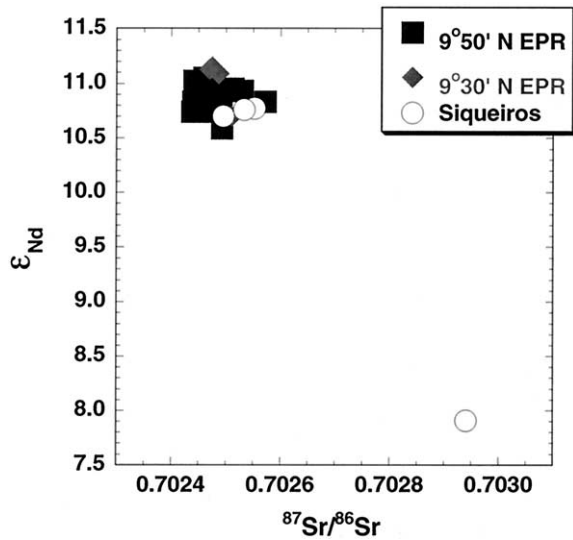


Fig. 2. ϵ_{Nd} vs. $^{87}\text{Sr}/^{86}\text{Sr}$ for axial 9 to 10°N and Siqueiros Transform samples measured in this study. Analytical uncertainties are similar to symbol size. EPR = East Pacific Rise.

increase with increasing $\text{Mg}^\#$ (Fig. 8) and decrease with increasing Na_g , La/Yb , and Sm/Nd fractionation (Fig. 9).

3.3.1. ^{235}U - ^{231}Pa

$^{231}\text{Pa}/^{235}\text{U}$ is > 1 in all of the axial 9 to 10°N samples (Fig. 7) (hereafter, $^{231}\text{Pa}/^{235}\text{U} > 1$ is referred to as ^{231}Pa excess). The relative values of these disequilibrium ratios give an order of partition coefficient incompatibility of $D_{\text{Ra}} < D_{\text{Pa}} < D_{\text{Th}} < D_{\text{U}}$. Unlike $^{230}\text{Th}/^{238}\text{U}$ and $^{226}\text{Ra}/^{230}\text{Th}$, $^{231}\text{Pa}/^{235}\text{U}$ is essentially constant for all of these samples.

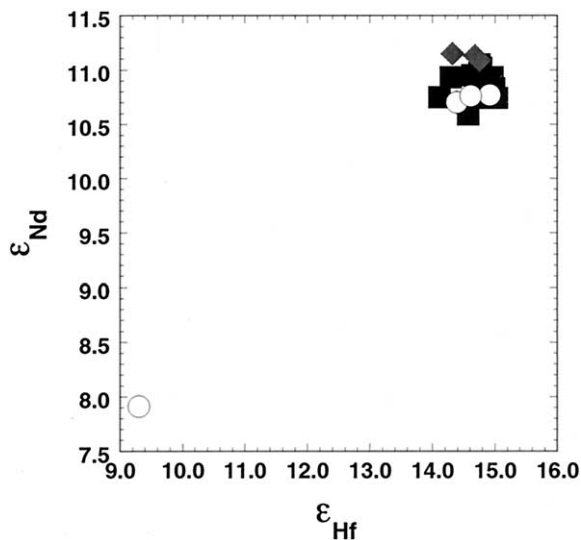


Fig. 3. ϵ_{Nd} vs. ϵ_{Hf} for axial 9 to 10°N and Siqueiros Transform samples measured in this study. Analytical uncertainties are similar to symbol size.

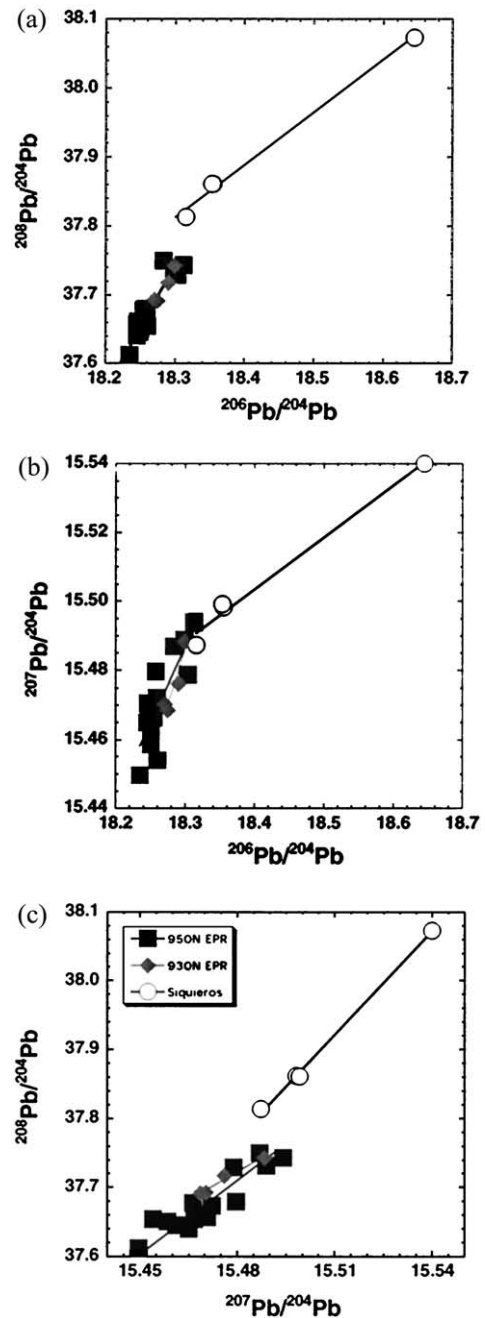


Fig. 4. (A) $^{208}\text{Pb}/^{204}\text{Pb}$ vs. $^{206}\text{Pb}/^{204}\text{Pb}$, (B) $^{207}\text{Pb}/^{204}\text{Pb}$ vs. $^{206}\text{Pb}/^{204}\text{Pb}$, and (C) $^{208}\text{Pb}/^{204}\text{Pb}$ vs. $^{207}\text{Pb}/^{204}\text{Pb}$ for axial 9 to 10°N and Siqueiros Transform samples. Analytical uncertainties (< 400 ppm; 2σ) are similar to symbol size. EPR = East Pacific Rise.

4. INTERPRETATION OF U-SERIES DATA FROM THE NORTHERN EPR

4.1. Background

MORB petrogenesis can be described in terms of several rate-dependent parameters, including the velocity of the upwelling mantle, the rate of melting, the melt velocity associated with melt extraction, and the delay time, or crustal storage time, of magma before eruption (e.g., Stolper et al., 1981; Turcotte,

Table 3. ($^{230}\text{Th}/^{232}\text{Th}$); ($^{230}\text{Th}/^{238}\text{U}$); ($^{226}\text{Ra}/^{230}\text{Th}$); ($^{231}\text{Pa}/^{235}\text{U}$); ($^{234}\text{U}/^{238}\text{U}$); and U, Th, Pa and Ra concentrations measured by thermal ionization mass spectrometry (TIMS), (SIMS) and inductively coupled plasma mass spectrometry (ICPMS).

Sample	[Th] (ug/g)	[U] (ug/g)	Th/U	$^{238}\text{U}/^{232}\text{Th}$	$^{230}\text{Th}/^{232}\text{Th}$	$^{230}\text{Th}/^{238}\text{U}$	^{231}Pa (fg/g)	$^{231}\text{Pa}/^{235}\text{U}$	[^{226}Ra] (fg/g)	$^{226}\text{Ra}/^{230}\text{Th}$	$^{234}\text{U}/^{238}\text{U}$
2359-4	0.1384 ^a	0.0542 ^a	2.552	1.189	1.376 ^b	1.157	46.23	2.62	49.23	2.04	1.002 ^b
2497-1b	0.1394 ^a	0.0560 ^a	2.489	1.219	1.425 ^b	1.169	n.d.	n.d.	51.67	2.34	1.003 ^b
2359-5	0.1575 ^a	0.0617 ^a	2.553	1.189	1.378 ^b	1.159	52.98	2.64	n.d.	n.d.	1.005 ^b
2368-4 (1)	0.1118 ^a	0.0456 ^a	2.449	1.239	1.411 ^a	1.139	37.36	2.52	47.34	2.70	1.002 ^a
2368-4 (2)	0.1116 ^a	0.0456 ^a	2.447	1.240	1.405 ^a	1.133			49.04	2.80	
2368-4 (avg) ¹	0.1117	0.0456	2.448	1.239	1.408	1.136			48.19	2.75	
2372-1	0.1176 ^a	0.0476 ^a	2.469	1.229	1.376 ^b	1.123	42.00	2.71	52.03	2.89	1.002 ^b
2392-9 (1)	0.1180 ^a	0.0479 ^a	2.466	1.230	1.390 ^a	1.130	38.97	2.50	48.83	2.67	1.001 ^a
2392-9 (2)	0.1174 ^a	0.0476 ^a	2.467	1.230	1.395 ^a	1.135			48.24	2.65	
2392-9(3)	0.1176 ^b	0.0478 ^b	2.460	1.233	1.394 ^b	1.131					1.03 ^b
2392-9 (avg) ¹	0.1177	0.0478	2.464	1.231	1.393	1.131			48.54	2.66	1.002
2752-6 (1)	0.1318 ^a	0.0518 ^a	2.546	1.192	1.362 ^a	1.143	40.99	2.43			1.002 ^a
2752-6 (2)	0.1315 ^a	0.0510 ^a	2.582	1.175	1.362 ^a	1.159			52.58	2.63	
2752-6 (avg) ¹	0.1317	0.0514	2.564	1.184	1.362	1.151					
2504-1	0.1183 ^a	0.0482 ^a	2.451	1.238	1.380 ^a	1.115	39.81	2.54	49.94	2.75	1.003 ^a
2351-2	0.1152 ^a	0.0460 ^a	2.505	1.211	1.368 ^b	1.129	n.d.	n.d.	50.37	2.86	1.001 ^b
2746-4 (1)	0.1236 ^a	0.0499 ^a	2.477	1.225	1.393 ^a	1.137	40.80	2.52	50.89	2.65	1.003 ^a
2746-4 (2)	0.122 ^a	0.0493 ^a	2.480	1.223	1.386 ^a	1.133					
2746-4 (avg) ¹	0.1229	0.0496	2.479	1.224	1.390	1.135					
2746-3b (1)	0.1130 ^a	0.0461 ^a	2.451	1.238	1.397 ^a	1.128	38.48	2.56	49.83	2.83	1.002 ^a
2746-3b (2)	0.1123 ^a	0.0456 ^a	2.463	1.232	1.423 ^a	1.154			48.85	2.75	
2746-3b (avg) ¹	0.1127	0.0459	2.457	1.235	1.410	1.142			49.34	2.79	
2370-6	0.1225 ^a	0.0493 ^a	2.482	1.223	1.360 ^a	1.112	40.31	2.51	49.65	2.68	1.003 ^a
2370-1 (1)	0.1534 ^a	0.0592 ^a	2.592	1.170	1.385 ^a	1.183	48.35	2.51			1.002 ^a
2370-1 (2)	0.1608 ^a	0.0617 ^a	2.609	1.163	1.390 ^a	1.195			49.79	2.01	1.001 ^a
2370-1 (avg) ¹	0.1571	0.0604	2.601	1.167	1.388	1.190					1.002
2355-8(1)	0.1469 ^a	0.0579 ^a	2.537	1.196	1.386 ^a	1.159	48.98	2.60	47.88	2.11	
2355-8(2)	0.1477 ^b	0.0581 ^b	2.542	1.192	1.376 ^b	1.153					1.001 ^b
2355-8(avg)	0.1473	0.0580	2.540	1.194	1.381	1.156					
2356-7(1)	0.1440 ^a	0.0568 ^a	2.537	1.196	1.386 ^a	1.159	49.50	2.68	48.99	2.21	
2356-7(2)	0.1432 ^b	0.0564 ^b	2.540	1.194	1.379 ^b	1.154					1.004 ^b
2356-7(avg)	0.1437	0.0566	2.538	1.195	1.380	1.156					
2361-6	0.1049	0.0420	2.495	1.216	1.388 ^b	1.142	n.d.	n.d.	40.14	2.48	1.002 ^b
2352-2(1)	0.1528 ^a	0.0601 ^a	2.542	1.194	1.382 ^a	1.158	51.25	2.62	52.96	2.25	
2352-2(2)	0.1512 ^b	0.0593 ^b	2.550	1.190	1.383 ^b	1.163					1.004 ^b
2352-2(avg)	0.1520	0.0597	2.546	1.192	1.383	1.160					
2358-3	0.1690 ^a	0.0658 ^a	2.568	1.181	1.376 ^b	1.165	55.02	2.57	n.d.	n.d.	1.005 ^b
2358-4	0.1688 ^a	0.0680 ^a	2.482	1.222	1.430 ^b	1.170	56.19	2.54	59.62	2.22	1.003 ^b
2365-3	0.1690 ^a	0.0664 ^a	2.546	1.192	1.381 ^b	1.159	56.15	2.60	57.00	2.20	1.003 ^b
TML 1LANL	30.26 ^a	10.80 ^a	2.801	1.083	1.086 ^a	1.003			3,623	0.991	1.004 ^a
TML- 2LANL	30.49 ^a	10.87 ^a	2.804	1.082	1.072 ^a	0.991			3,635	0.999	
TML 1WHOI	29.45 ^b	10.543 ^b	2.793	1.086	1.084 ^b	0.997					1.004 ^b
TML 2WHOI	29.44 ^b	10.517 ^b	2.799	1.084	1.084 ^b	0.999					1.002 ^b
TML 3WHOI	30.17 ^b	10.695 ^b	2.821	1.076	1.082 ^b	1.006					1.005 ^b

¹ Duplicate measurements represent separate glass splits; glass samples were leached on the ship in 6 N HCl for 15 min, hand picked under a microscope in the lab, then ultrasonically leached in sequential treatments of 1 N HCl plus 2% H₂O₂ (15 min), DI water (twice, each time for 15 min), 0.1 N oxalic acid plus 2% H₂O₂, DI water (twice, each time for 15 min), acetone (15 min). Samples were then hand picked by microscope for a second time. Sample splits (>1 g) were then dissolved, aliquoted, spiked, and then U-Th-Pa and Ra were separated using chemical techniques outlined in Goldstein et al., (1989), Volpe et al., (1993), Pickett et al., (1996) and Layne and Sims (2000).

² [U], [Th], measured by both (a) ID-TIMS at LANL and (b) ID-ICP-MS at WHOI; measurement errors for [U], [Th] ≤ 0.8% (2σ) for ID-TIMS and ≤ 1.0% for ID-ICP-MS

³ () denotes activity $\lambda_{238} = 1.551 \times 10^{-10} \text{ yr}^{-1}$; $\lambda_{232} = 4.948 \times 10^{-11} \text{ yr}^{-1}$ errors (2σ) range from 0.4 to 1.0% and do not include uncertainties in λ_{238} (0.07%) or λ_{232} (0.5%).

⁴ $^{232}\text{Th}/^{210}\text{Th}$ measured by (a) HAS-TIMS at LANL (Goldstein et al., 1989) and (b) SIMS at WHOI (Layne and Sims, 2000); activity ratios calculated using $\lambda_{230} = 9.195 \times 10^{-6} \text{ yr}^{-1}$ and $\lambda_{232} = 4.948 \times 10^{-11} \text{ yr}^{-1}$; errors (2σ) range from 0.6 to 1.2% for both techniques and do not include uncertainties in λ_{230} (0.4%) or λ_{232} (0.5%).

⁵ [^{226}Ra] measured by ID-TIMS at LANL (Volpe et al., 1991; $\lambda_{226} = 4.331 \times 10^{-4} \text{ yr}^{-1}$; errors (2σ) range from 1.2 to 3.6% and do not include uncertainties in λ_{226} (0.4%) or λ_{230} .

⁶ [^{231}Pa] measured by ID-TIMS at LANL (Pickett et al., 1996); $\lambda_{231} = 2.115 \times 10^{-5} \text{ yr}^{-1}$; errors (2σ) range from 1.0 to 3.0% and do not include uncertainties in λ_{231} (0.4%) or λ_{235} (0.07%).

⁷ $^{234}\text{U}/^{238}\text{U}$ measured by (a) TIMS at LANL and (b) ICP-MS at WHOI; $\lambda_{234} = 2.823 \times 10^{-6} \text{ yr}^{-1}$; errors (2σ) < 1.0%; for these samples $^{234}\text{U}/^{238}\text{U} = 1$ within error using an equilibrium $^{234}\text{U}/^{238}\text{U}$ of 54.95 ppm. For ICP-MS NBS 960 was run between each sample to determine mass bias.

⁸ TML was used to calibrate ^{233}Pa spike, but measured as an unknown for U-Th-Ra disequilibria.

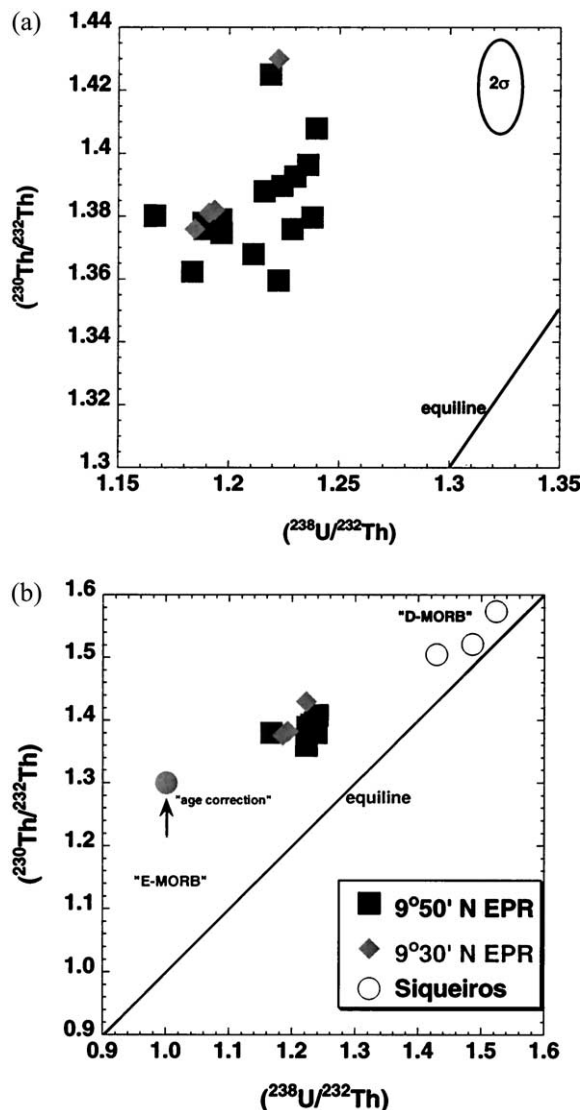


Fig. 5. (A) U/Th vs. $^{230}\text{Th}/^{232}\text{Th}$ for axial 9 to 10°N samples. Error ellipse represents maximum analytical uncertainty. (B) U/Th vs. $^{230}\text{Th}/^{232}\text{Th}$ for axial 9 to 10°N samples and Siqueiros Transform samples (Lundstrom et al., 1998) for which Nd, Sr, Hf, and Pb isotopes have been measured. Note that the age of Siqueiros E-type sample (2390-1) is thought to be significant relative to the half-life of ^{230}Th (Lundstrom et al., 1999). The age correction for this sample comes from Lundstrom et al. (1999) and is based upon the method of Goldstein et al. (1992, 1993). This correction assumes that the Siqueiros sample (2391) and the near axis 9°37 E-MORB (mid-ocean ridge basalt) (R54-2), from Volpe and Goldstein (1993), erupted with the same $^{230}\text{Th}/^{232}\text{Th}$. EPR = East Pacific Rise.

1982; McKenzie, 1984, 1985; Richter and McKenzie, 1984; Ribe, 1985, 1987, DePaolo, 1996). While the velocity of solid upwelling mantle can be estimated from the mid-ocean ridge spreading rate or other geophysical measurements, (e.g., McKenzie and Bickle, 1988; Watson and McKenzie, 1991; Forsyth, 1992), there are few constraints on the other parameters that control the time scales of melt generation and transport in the mantle. For this reason, it is desirable to pursue other approaches to constrain the rate-dependent parameters of MORB petrogenesis. U-decay series nuclides have half-lives that are

comparable to the time scales of melt generation and transport. Because of their appropriate half-lives and because radioactive steady-state requirements constrain the abundances and activities of decay series before chemical fractionation (Bateman, 1910), measurement of disequilibria among the isotopes of the U and Th decay series can provide unique and direct constraints on the timing and extent of chemical fractionation occurring during magma genesis (e.g., McKenzie, 1984; Condomines et al., 1988; Spiegelmen and Elliott, 1993).

In almost all young MORB, $^{230}\text{Th}/^{238}\text{U}$, $^{231}\text{Pa}/^{235}\text{U}$, and/or $^{226}\text{Ra}/^{230}\text{Th}$ are > 1 , indicating that ^{230}Th has been significantly enriched in the melt relative to ^{238}U (^{230}Th excesses range from 1.0 to 1.35), ^{226}Ra has been enriched relative to ^{230}Th (^{226}Ra excesses range from 1.0 to 4.0), and ^{231}Pa has been enriched relative to ^{235}U (^{231}Pa excesses range from 2.3 to 2.8). On the basis of measurements of mineral-melt partition coefficients, the observed ^{230}Th excesses measured in MORB have been interpreted as requiring melt extraction to begin deep, at pressures > 1.5 GPa, either in the presence of garnet or near-solidus pyroxene (LaTourrette and Burnett, 1992; Beattie, 1993a, 1993b; LaTourrette et al., 1993; Wood et al., 1999; Landwehr et al., 2001). Because the parent elements, U and Th, are thought to be highly incompatible, the large ^{230}Th , ^{231}Pa , and ^{226}Ra excesses suggest that either (a) melting is near fractional and the melting rate is low compared to the half-lives of ^{230}Th , ^{231}Pa , and ^{226}Ra ; or (b) melt extraction processes involve porous flow at very small intergranular porosities. In both scenarios, the absolute value of the melt fractions and/or intergranular porosities that are required depends strongly on the mineral-melt partitioning values for U and Th.

Determining the rate-dependent parameters of MORB petrogenesis from U-series measurements requires knowledge of the nature of melt extraction and the degree of chemical equilibrium between melt and solid during melt transport. Constraints from the chemistry of erupted magmas (Klein and Langmuir, 1987; Langmuir et al., 1992), exposed ophiolites (Nicolas, 1986; Kelemen et al., 1995), abyssal peridotites (Dick et al., 1984; Johnson et al., 1990; Johnson and Dick, 1992; Niu, 1997), and physical models have led to two end-member theories of melt generation and transport. One, "dynamic melting," considers melting a near fractional process in which melt is chemically isolated from the solid matrix and transported to the surface as soon as a critical threshold porosity is attained (Langmuir et al., 1977; McKenzie, 1984). The other, "reactive porous flow," considers melting and melt transport a reactive process in which melt percolates through a porous matrix, undergoing chemical exchange (Navon and Stolper, 1987; Spiegelmen and Elliott, 1993). Because these two end-member models attribute $^{226}\text{Ra}/^{230}\text{Th}$ and $^{230}\text{Th}/^{238}\text{U}$ to different processes, the relationship between these two disequilibria is one of the key pieces of evidence that can be used to choose between these different models.

In dynamic melting, ^{226}Ra and ^{230}Th excesses are both generated at the bottom of the melt column, near the peridotite solidus, and decrease with increasing degrees of melting and decompression. ^{226}Ra and ^{230}Th excesses are therefore expected to be positively correlated in primary magmas. Fast melt transport through conduits or channels is required to maintain the observed disequilibria before the excess daughter elements can decay back to equilibrium. Because of the short half-life of

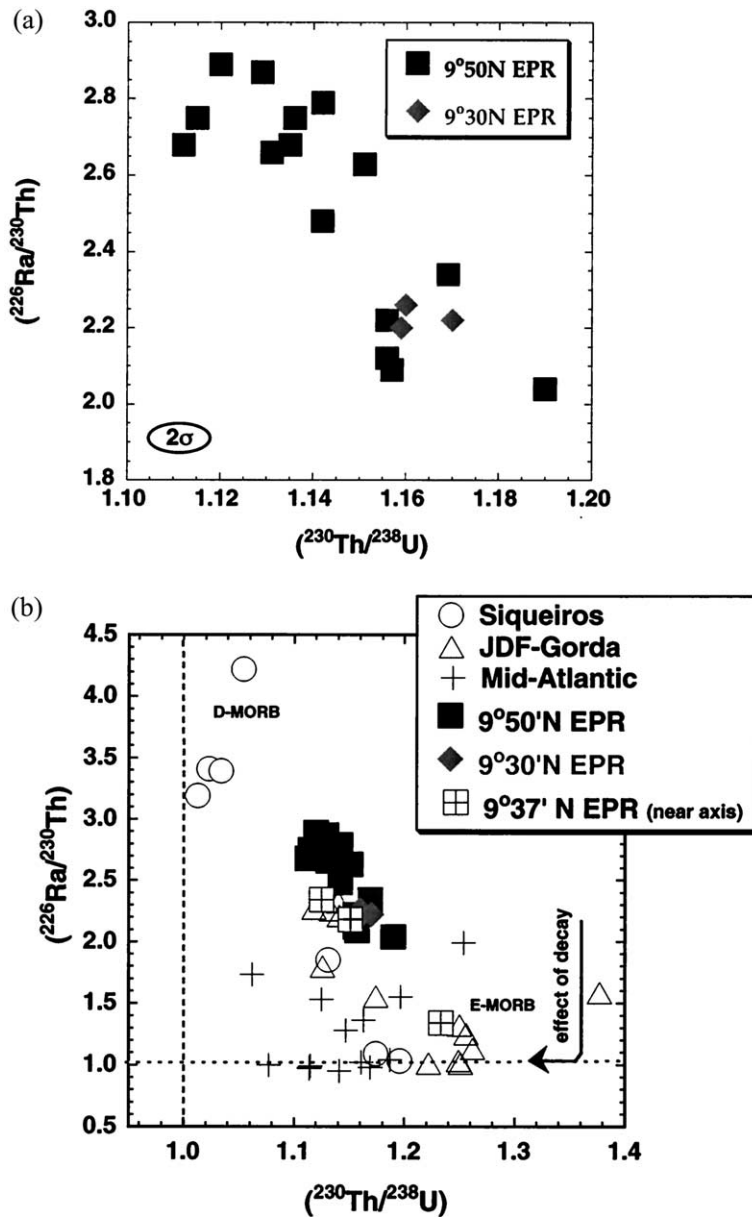


Fig. 6. (A) $^{230}\text{Th}/^{238}\text{U}$ vs. $^{226}\text{Ra}/^{230}\text{Th}$ for axial 9 to 10°N samples measured in this study. Error bars incorporate uncertainties in the analytical measurements and sample eruption ages (± 100 yr). Double-error regression (using the bootstrap method of Sohn and Menke, in press) gives a weighted linear correlation coefficient of 0.84 ± 0.07 , -0.17 at the 90% confidence limit, indicating that this correlation is not random. (B) ^{230}Th vs. ^{226}Ra for the global midocean ridge basalt (MORB) data set. Axial 9 to 10°N samples come from this study; two axial 9 to 10°N samples (replicated in this study; Table 3) are from Lundstrom et al. (1999); three “near-axis” East Pacific Rise (EPR) samples, including one E-type from close to the 9°37'N DEVAL, come from Batiza and Niu (1992) and Volpe and Goldstein (1993); Juan de Fuca (JDF) and Gorda ridge samples are from Volpe and Goldstein (1993) and Goldstein et al. (1989); Mid-Atlantic ridge samples are from Lundstrom et al. (1998); and Siqueiros Transform samples are from Lundstrom et al. (1999). Note that two earlier alpha counting EPR data sets that have both ^{226}Ra and ^{230}Th data (Rubin and Macdougall, 1988; Reinitz and Turekian, 1989) were not included. Because of the significant difference in the half-lives of ^{226}Ra and ^{230}Th , ^{226}Ra excesses decay back to equilibrium long before ^{230}Th excesses (note decay curve on plot). Except for the axial 9 to 10°N samples from this study and the Siqueiros D-type MORBs, the samples comprising the global MORB Th-Ra data set have been collected by dredging. As a result, before this work, Th-Ra systematics for MORBs were in question.

^{226}Ra , if Th-Ra disequilibrium in MORB was produced at the bottom of the melt column, by melting of garnet lherzolite, then a very rapid magma ascent rate would be required to preserve the ^{226}Ra excess; this would provide a strong constraint on melt transport.

The reactive porous flow model, on the other hand, does not require the ^{226}Ra excesses to be generated near the solidus at the bottom of the melt column, since daughter Ra is more incompatible than parent Th in both spinel and garnet lherzolite facies rocks (Beattie, 1993a, 1993b; Blundy and Wood, 1994;

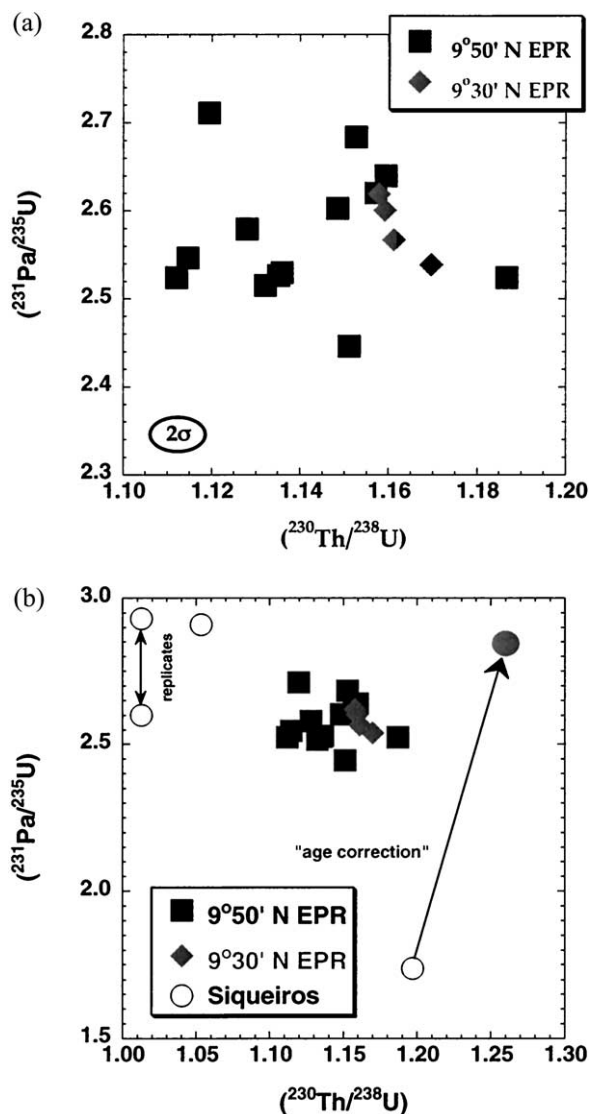


Fig. 7. (A) $^{230}\text{Th}/^{238}\text{U}$ vs. $^{231}\text{Pa}/^{235}\text{U}$ for axial 9 to 10°N samples (study). Error ellipse represents maximum analytical uncertainties. (B) $^{230}\text{Th}/^{238}\text{U}$ vs. $^{231}\text{Pa}/^{235}\text{U}$ for the axial 9 to 10°N and Siqueiros samples. Age correction for the Siqueiros E-type sample (2390-1) comes from Lundstrom et al. (1999) and is based upon the method of Goldstein et al. (1989). Replicate values for $^{231}\text{Pa}/^{235}\text{U}$ of Siqueiros sample 2384-1 are as reported in Lundstrom et al. (1999). EPR = East Pacific Rise.

Sims et al., 1999; Cooper et al., 2000). Slower melt migration through the porous matrix and chromatographic exchange with the residual solid maintains the ^{226}Ra excess to shallow levels within the melt column (e.g., see Spiegelmen and Elliott, 1993). With this model, melt transport is not constrained to be fast and can be calculated explicitly from the U-series measurements. Because experimental data on U-Th partitioning suggest that the large ^{230}Th excesses measured in MORB require deep melt extraction (Landwehr et al., 2001), all MORB melt cannot have reequilibrated to shallow levels. Therefore, because of the large Th excesses observed in most MORB, reactive porous flow cannot be the only mechanism of melt transport.

Before this work, there had been four axial MORB suites

measured for both ^{230}Th and ^{226}Ra (Fig. 6) by mass spectrometric methods: (a) a suite of dredge samples from the Juan de Fuca and Gorda ridges (Volpe and Goldstein, 1993), (b) a suite of dredge samples from the Mid-Atlantic Ridge (Lundstrom et al., 1998), (c) a limited suite of three near-axial dredge samples from 9°37'N along the EPR (Volpe and Goldstein, 1993), and (d) a suite of *Alvin* and dredge samples from the Siqueiros Transform (Lundstrom et al., 1999). No clear systematics emerge for the Atlantic Th-Ra data, probably because of the highly variable age of dredged samples from this slow-spreading ridge. In MORB from the Juan de Fuca Ridge and the Siqueiros Transform and northern EPR, Th and Ra excesses are negatively correlated (Volpe and Goldstein, 1993; Kelemen et al., 1997; Lundstrom et al., 1995, 1999). This is unlike ocean island basalts, such as those in Hawaii, which show positive correlations between Th, Pa, and Ra excesses and the degree of partial melting (Sims et al., 1999).

To account for the negative correlation between ^{230}Th and ^{226}Ra excesses, it has been proposed that melt with a ^{230}Th excess forms near the base of the melting region and then ascends rapidly in chemically isolated conduits, while slow, reactive transport forms ^{226}Ra excess at shallow levels in the mantle (Kelemen et al., 1997; Sims et al., 1998; Lundstrom et al., 1999). A similar "two-porosity" system was previously proposed by Iwamori (1993, 1994) to account for trace element systematics in MORB and abyssal peridotites.

This hypothesis relies on the assumptions that ^{230}Th - ^{226}Ra disequilibria measured in the MORB is primary and that both sample ages and crustal residence times are negligible relative to the half-life of ^{226}Ra . However, the observed negative correlation between ^{226}Ra and ^{230}Th was based primarily on dredge samples (e.g., the Juan de Fuca and Gorda ridge samples), and because end-member samples with the highest ^{230}Th excesses and smallest ^{226}Ra excesses (e.g., the Siqueiros E-type lavas) may be old, relative to the half-life of ^{226}Ra (and probably even ^{231}Pa), the extent to which this correlation is a primary feature of melting is uncertain. Furthermore, because limited measurements of Nd and Sr isotopes in these samples have shown that they were derived from relatively heterogeneous sources (Natland, 1989; Rubin and MacDougall, 1992; Sims et al., 1995), it has been difficult to determine the extent to which U-series variations in these suites reflect variations in melting processes vs. variations in source lithology (e.g., garnet pyroxenite, garnet peridotite, spinel peridotite) (e.g., see Lundstrom et al., 1995, 1999, 2000; Condomines and Sigmarsson, 2000). In this work, we are certain that the samples analyzed have erupted exclusively within the axial summit trough, and their ages are demonstrably young, if not known absolutely (e.g., 1991 to 1992 eruption; Haymon et al., 1993; Rubin et al., 1994). Furthermore, measurements of Sr, Nd, Pb, and Hf isotopes (Table 2) indicate that they were derived from long-term depleted sources that are nearly identical or only slightly heterogeneous in terms of their incompatible element abundances.

4.2. Constraints on Long-Term Sources of Axial 9 to 10°N Axial Lavas

^{230}Th excesses in basalts are highly dependent on bulk partition coefficients for U and Th and therefore the mineralogy of mantle sources. While several models relating U-series dis-

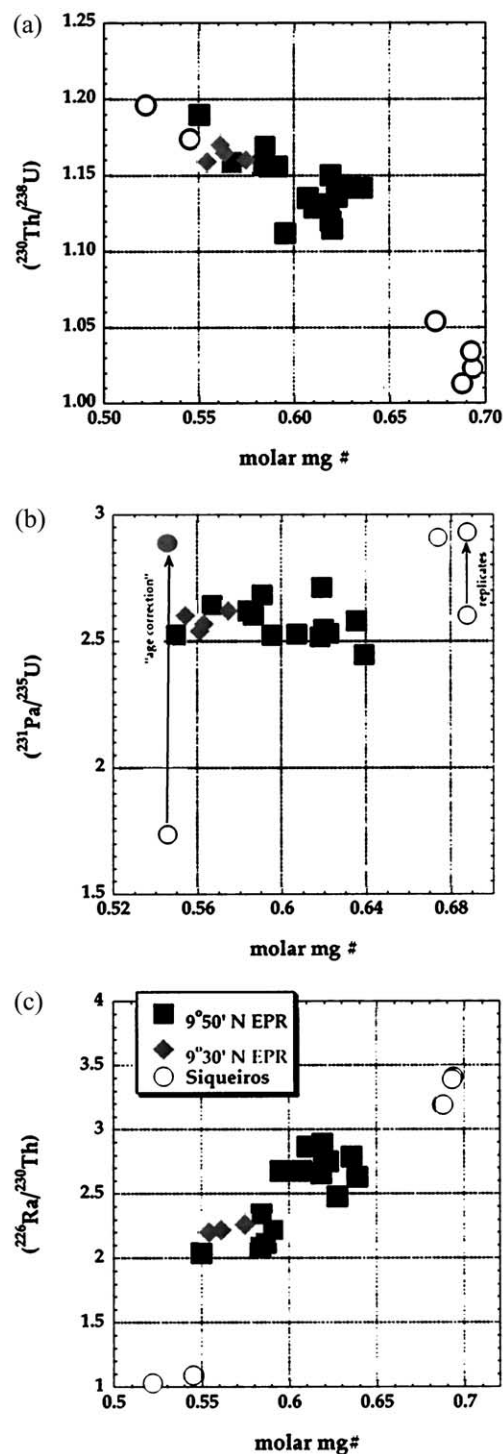


Fig. 8. (A) ^{230}Th excess vs. $\text{Mg}^\#$ (molar $\text{Mg}/[\text{Mg} + \text{Fe}]$) for the axial 9 to 10°N and Siqueiros Transform samples. Double-error regression (Sohn and Menke, in press) gives a slope of -0.97 ± 0.2 and an intercept of 1.7 ± 0.2 , with a weighted linear correlation coefficient (r_{xy}) of -0.87 , which falls on the interval of $-0.94 \leq r_{xy} \leq -0.77$ at the 90% confidence limit. (B) ^{231}Pa excess vs. $\text{Mg}^\#$ for the 9 to 10°N and Siqueiros data. (C) ^{226}Ra excess vs. $\text{Mg}^\#$ for the axial 9 to 10°N and Siqueiros Transform samples. Error bars include both analytical and eruption age uncertainties. Double-error regression (Sohn and Menke, in press) gives a slope of 15 ± 6 and an intercept of -7 ± 4 , with a weighted linear correlation coefficient (r_{xy}) of -0.65 , which falls in the interval of $-0.50 \leq r_{xy} \leq -0.84$ at the 90% confidence limit. EPR = East Pacific Rise.

equilibria to melting of a homogeneous peridotite have been proposed (e.g., McKenzie, 1985; Spiegelman and Elliott, 1993), it has also been suggested that variations observed in the U-Th disequilibrium can be explained by mixing of melts derived from different lithologies that have distinctive long-term chemical characteristics (Ben Othman and Allegre, 1990; Lundstrom et al., 1995, 1999, 2000; Condomines and Sigmarsson, 2000).

It was originally thought that the large ^{230}Th excesses measured in MORB samples required melt extraction in the presence of garnet (LaTourrette and Burnett, 1992; Beattie, 1993a, 1993b; LaTourrette et al., 1993). However, recent studies have shown that at or near solidus conditions, Th may also be more incompatible than U during melting in the presence of high-temperature, high-pressure clinopyroxene (Wood et al., 1999; Landwehr et al., 2001). This would suggest that melting of spinel peridotite at pressures $> \sim 1.5$ GPa could also cause ^{230}Th excesses. While these new results appear to relax the requirement that ^{230}Th excesses require melting in the presence of garnet, Wood et al.'s (1999) clinopyroxene U-Th partition coefficients still require Th excesses to be generated deep (> 1.5 GPa). In addition, they conclude that the large values of ^{230}Th excess in MORB "are unlikely to have been produced by melting of spinel lherzolite, and that garnet lherzolite is a more plausible source" (Landwehr et al., 2001, p. 346).

Because very few suites measured for U-series disequilibrium have also been measured for Hf, Nd, Sr, and Pb isotopes, the extent to which U-series disequilibrium reflect variations in the melting processes, as opposed to variable mixing of melts from depleted (peridotitic) and enriched (pyroxenitic) sources, is not well constrained. The Hf, Nd, and Sr isotopic ratios measured in our very young axial 9 to 10°N lava suite are essentially constant within analytical uncertainty and therefore not correlated with the observed ^{230}Th excesses (Figs. 10A to 10B). These isotope ratios indicate that all of the samples come from a homogeneous mantle source that is depleted with respect to Sm/Nd, Lu/Hf, and Rb/Sr. Furthermore, as will be discussed later, when comparing the axial 9 to 10°N samples with the Siqueiros end-member D-MORB and E-MORB samples, the axial 9 to 10°N N-MORB cannot be explained by binary mixing of melts from depleted and enriched sources, as proposed by Lundstrom et al. (1999).

In contrast, the Pb isotopic ratios of the axial 9 to 10°N samples are variable. This variation is larger than the analytical uncertainties of the high-precision MC-ICP-MS measurements, but it is limited when compared to adjacent segments of the EPR (e.g., White, 1985; Galer et al., 2000). This variability is linear and well correlated, suggesting that there is some variation in the time-integrated U/Pb and Th/Pb mantle sources of these samples. The extent to which this Pb isotopic variation also reflects differences in Th/U source ratios is critical to the interpretation of the U-series data. In this regard, it is important to note that for our axial 9 to 10°N samples, $^{208}\text{Pb}/^{206}\text{Pb}$, which represents the time-integrated Th/U ratio of the mantle source, is essentially constant and independent of the samples' ^{230}Th excesses (Fig. 10D). When compared to simple single- and two-stage Pb evolution models, which consider the time-integrated U/Th/Pb of the mantle source (Holmes, 1946; Houtermans, 1946; Galer and O'Nions, 1985; Elliot et al., 1999), the nearly constant $^{208}\text{Pb}/^{206}\text{Pb}$ compositions of these samples suggest that they came from a mantle source that is homoge-

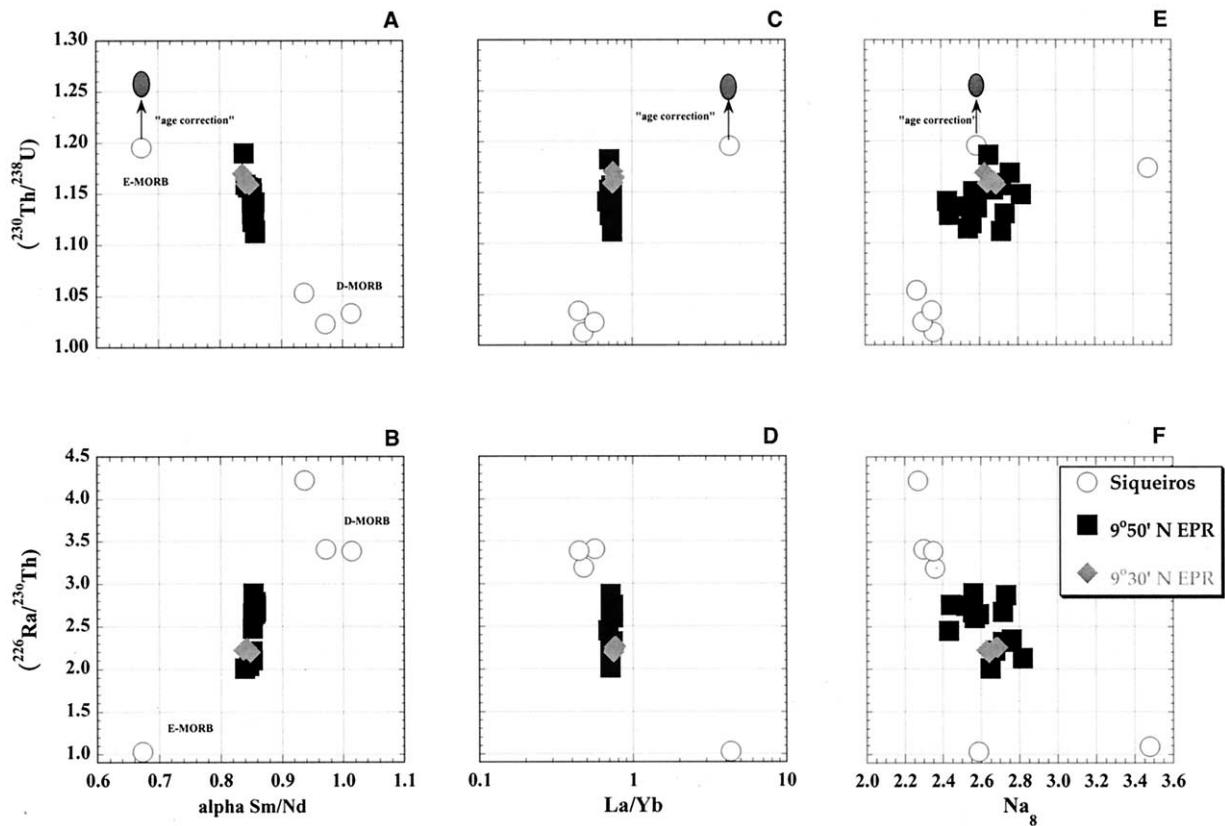


Fig. 9. (A) ^{230}Th excess and (B) ^{226}Ra excess vs. alpha Sm/Nd for axial 9 to 10°N and Siqueiros Transform samples. Alpha Sm/Nd is a measure of the Sm/Nd fractionation during midocean ridge basalt (MORB) petrogenesis and is the Sm/Nd concentration ratio measured in the lava normalized to a model Sm/Nd source ratio inferred from the $^{143}\text{Nd}/^{144}\text{Nd}$ of the lavas (for details, see DePaolo, 1988; Salters and Hart, 1989; Sims et al., 1995). Although the variance in the calculated alpha Sm/Nd for the axial 9 to 10°N lavas, measured by isotope dilution, is similar to the analytical uncertainties, the isotope dilution data suggest correlations with ^{230}Th and ^{226}Ra excesses consistent with those observed in the larger data set, which includes the Siqueiros Transform D-MORBs and E-MORBs. (C) ^{230}Th excess and (D) ^{226}Ra excess vs. La/Yb for axial 9 to 10°N and Siqueiros Transform samples. For the axial 9 to 10°N samples, the variance in La/Yb, measured by inductively coupled plasma mass spectrometry, is much smaller than the propagated analytical uncertainties. (E) ^{230}Th excess and (F) ^{226}Ra excess vs. Na_8 for axial 9 to 10°N and Siqueiros Transform samples. Na_8 was calculated using a linear regression of Na_2O vs. MgO in the axial 9 to 10°N samples. For lavas with >8.5 wt.% MgO , Na_8 is equal to the observed wt.% Na_2O . EPR = East Pacific Rise.

neous with respect to its time-integrated Th/U. For a single-stage Pb evolution model, the $^{208}\text{Pb}/^{206}\text{Pb}$ lava compositions predict a variation of $< 1\%$ in the Th/U source ratio of these samples. This 1% variation in Th/U inferred from the Pb isotope data is much smaller than the 6% variation in Th/U observed in our data (Fig. 11). Because these samples lie on a linear array in Pb isotope space, two-stage Pb evolution models would require that the Th/U ratio of their source was homogeneous. However, interpretation of the Pb isotope compositions of these samples in terms of a two-stage model also requires that the linear arrays in $^{207}\text{Pb}/^{204}\text{Pb}$ vs. $^{206}\text{Pb}/^{204}\text{Pb}$ represent secondary isochrons. In this case, the large slope of the our data array in $^{207}\text{Pb}/^{204}\text{Pb}$ vs. $^{206}\text{Pb}/^{204}\text{Pb}$ space would predict that the second stage of Pb evolution started very early in the Earth's history and that the mantle source of these lavas has remained closed ever since, a scenario which is highly unlikely.

In this regard, it is also important to note that the time-averaged Th/U inferred by the $^{208}\text{Pb}/^{206}\text{Pb}$, using both single-stage (Th/U ~ 3.7 to 3.8) and two-stage (Th/U ~ 3.1 to 3.6) Pb evolution models is different than the Th/U of the source

inferred from either the samples $^{230}\text{Th}/^{232}\text{Th}$ (Th/U ~ 2.12 to 2.24) or measured Th/U (2.45 to 2.60). This discrepancy between MORB's inferred long-term and more recent Th/U source ratios has been previously noted and is referred to as the "kappa conundrum" (cf. Galer and O'Nions, 1985; Elliot et al., 1999). To explain this kappa conundrum, several models have been proposed that require either a recent influx of Pb from the lower mantle (Galer and O'Nions, 1985) or a multistage evolution for Pb (Elliot et al., 1999).

Regardless of the interpretation of the Pb isotopic compositions of our samples (single-stage, two-stage, multistage, or open-system), their constant $^{208}\text{Pb}/^{206}\text{Pb}$ ratios suggest that our young axial samples come from a source with effectively constant time-integrated Th/U. Therefore, we conclude that the variation in the observed Th/U reflects elemental fractionation during melt generation and transport processes, rather than variability in the Th/U of the mantle source.

Most U-series measurements of MORB, including ours, show positive trends between $^{230}\text{Th}/^{238}\text{U}$ and Th/U for a given ridge segment (Goldstein et al., 1989, 1993; Reinitz

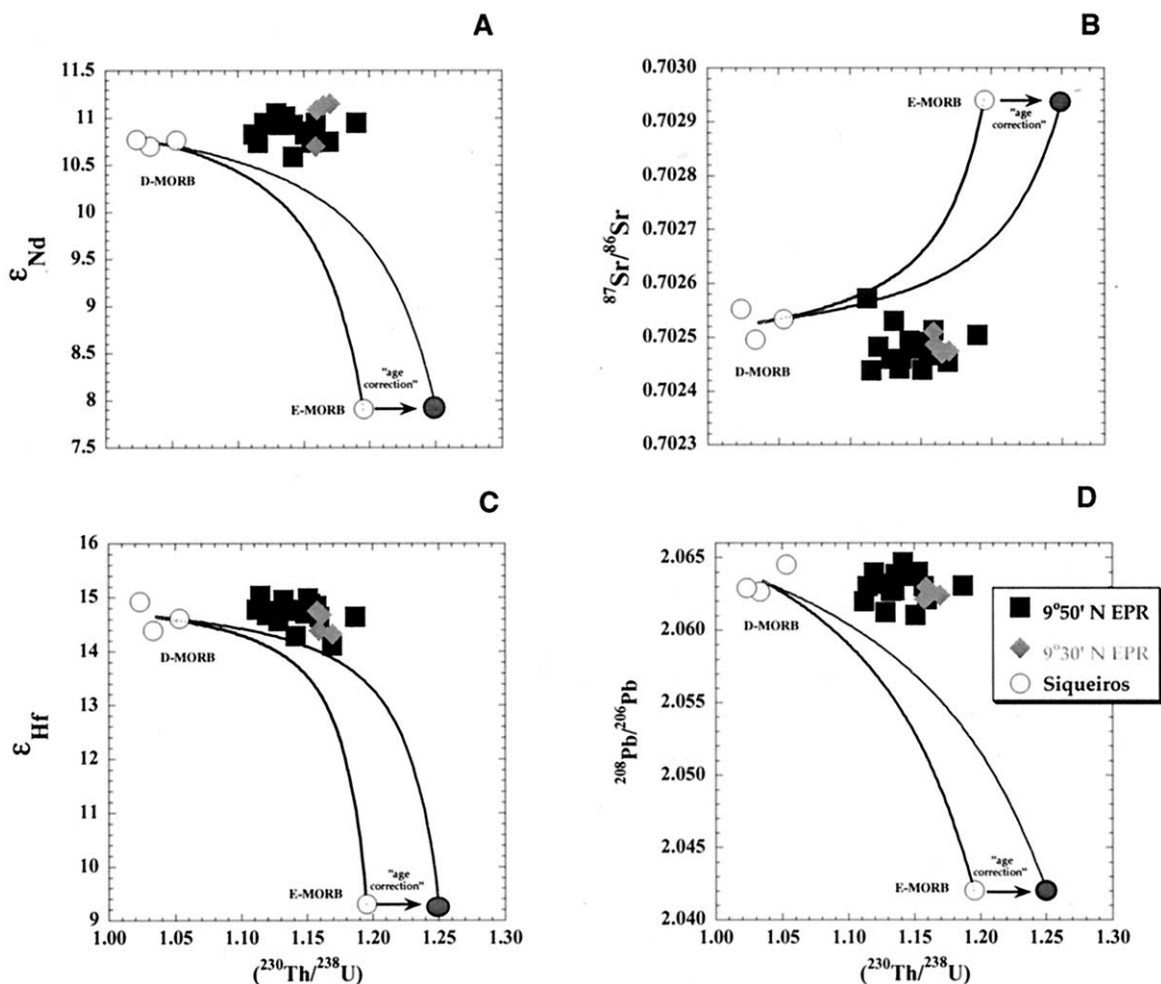


Fig. 10. ^{230}Th excess vs. (A) ϵ_{Nd} , (B) $^{87}\text{Sr}/^{86}\text{Sr}$, (C) ϵ_{Hf} , and (D) $^{208}\text{Pb}/^{206}\text{Pb}$ for the axial 9 to 10°N and Siqueiros Transform samples. Note that an unpublished $^{87}\text{Sr}/^{86}\text{Sr}$ analysis of ~ 0.7026 for the East Pacific Rise (EPR) near axial E-MORB (midocean ridge basalt), R54-2, reported in Batiza and Niu (1992) but not shown here, is similar to the values measured for the axial 9 to 10°N and Siqueiros Transform D-MORB samples. Inclusion of this sample in this data set would extend the range of ^{230}Th excess (1.23) for samples having similar $^{87}\text{Sr}/^{86}\text{Sr}$. For each plot, two possible mixing trends are shown. One uses the measured value for the end-member E-type Siqueiros lava, while the other uses the "age-corrected" value for the end-member E-type Siqueiros lava (Lundstrom et al., 1999) for the mixing calculations. Because of the large differences in the concentrations of Nd, Sr, Hf, Pb, U, and Th in the end-member Siqueiros D-MORB and E-MORB samples, these mixing curves are dominated by the E-MORB component and therefore do not pass through the axial 9 to 10°N data array.

and Turekian, 1989; Ben Othman and Allegre, 1990; Lundstrom et al., 1998). Because MORBs represent large degrees of partial melting, and Th and U have commonly been thought to be highly incompatible in mantle minerals, it has been proposed that the observed variations in Th/U reflect variation in mantle source composition (Lundstrom et al., 1995; 1998, 1999, 2000). In this view, the correlation between Th/U and the degree of $^{230}\text{Th}/^{238}\text{U}$ disequilibria (Fig. 11) is interpreted to reflect mixing of melts derived from enriched and depleted sources. The more enriched sources (higher Th/U) are small-scale, garnet-bearing mafic veins that produce greater amounts of ^{230}Th excesses because of the higher garnet abundance.

The constant Nd, Sr, Hf, and $^{208}\text{Pb}/^{206}\text{Pb}$ isotopic compositions measured in our samples suggest that the variations of Th/U and ^{230}Th and ^{226}Ra excesses are best explained by variability in melt generation and transport processes, not the mixing of enriched and depleted mantle melts, as has been

previously suggested (Lundstrom et al., 1999, 2000). Furthermore, if the E-MORB isotope signature documented in the Siqueiros E-MORB samples is representative of a melt component derived from garnet pyroxenite veins, then the lack of variability in the heavy isotope ratios within the 9 to 10°N axial sample suite can also be interpreted as evidence against mixing of enriched melts from garnet pyroxenite veins with melts derived from ambient peridotitic mantle (e.g., Ben Othman and Allegre, 1990; Lundstrom et al., 1999, 2000; Condomines and Sigmarsson, 2000).

4.3. Influence of Crustal Processes and Magma Storage Time on U-Series Disequilibria

There is considerable geophysical and geological evidence that suggests that MORBs reside in crustal, and perhaps subcrustal, axial magma chambers (AMCs) before

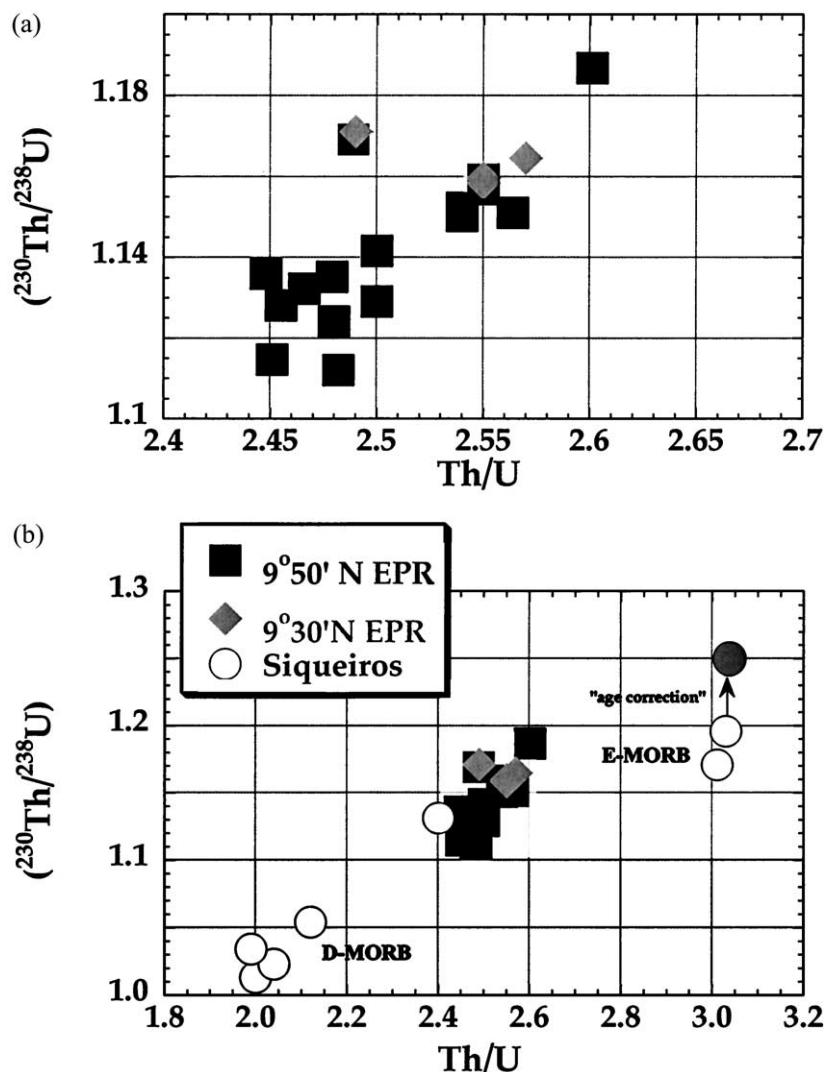


Fig. 11. (A) ^{230}Th excess vs. Th/U for the axial 9 to 10°N samples. (B) ^{230}Th excess vs. Th/U for the axial 9 to 10°N and Siqueiros Transform samples. EPR = East Pacific Rise.

eruption (e.g., Grove and Bryan, 1983; Detrick et al., 1987; Kent et al 1990; Toomey et al., 1990; Sinton and Detrick, 1992; Boudier and Nicolas, 1995; Kelemen et al., 1997; Dunn et al., 2000). Chemical data also imply that MORBs are chemically evolved as a result of crystal fractionation (e.g., O'Hara, 1968). Determining the time scales of magma storage and differentiation and the chemical influence of this crustal residence is critical to the interpretation of U-series disequilibria in our samples. If magma storage time is significant relative to the half-life of the daughter isotopes, then the daughter/parent activity ratios will decay toward their equilibrium values and cause us to infer too small an amount of daughter/parent fractionation during mantle petrogenesis. Similarly, if U-series disequilibria in our samples have been produced or modified by crustal processes (e.g., assimilation and fractional crystallization), then interpretation of the U-series data in terms of melting processes would also be incorrect.

The relationship between $\text{Mg}^\#$ and excesses of ^{226}Ra , ^{231}Pa , and ^{230}Th provides one means to assess the extent to which

crustal processes may have influenced the measured U-series disequilibria (Fig. 8). For our axial 9 to 10°N samples, ^{231}Pa excesses are constant as a function of $\text{Mg}^\#$, whereas ^{226}Ra excesses decrease and ^{230}Th excesses increase with decreasing $\text{Mg}^\#$. The simplest interpretation of the constant ^{231}Pa excesses and positive correlation between ^{226}Ra excesses and $\text{Mg}^\#$ is that the time scale of magma differentiation is of the same order of magnitude as the half-life of ^{226}Ra , but short compared to the half-life of ^{231}Pa . However, the negative correlation of ^{230}Th excesses and $\text{Mg}^\#$ is opposite from what would be expected for radioactive decay during magma storage. Also, the half-life of ^{230}Th is much longer than ^{226}Ra ; after a crustal storage time long enough for measurable ^{230}Th decay, there should be no measurable ^{226}Ra excess.

Interpretation of these data requires understanding how variations in excesses of ^{226}Ra and ^{230}Th are related to $\text{Mg}^\#$. As discussed above, these trends cannot be due to variations in source composition, unless the $\text{Mg}^\#$ and ^{230}Th and ^{226}Ra excesses are more sensitive indicators of source composition than

Nd, Sr, Hf, and Pb isotopes, which is unlikely. The three simplest possible explanations for the observed correlation between ^{226}Ra and ^{230}Th excesses and $\text{Mg}^\#$ are as follows: (a) The positive correlation between ^{226}Ra excesses and $\text{Mg}^\#$ reflects the time scale of magma differentiation, while the negative correlation between ^{230}Th excess and $\text{Mg}^\#$ reflects the influence of secondary crustal processes, such as assimilation or crystallization; (b) the variations in the ^{226}Ra and ^{230}Th excesses and $\text{Mg}^\#$ result from melt generation and transport processes; and (c) one or both of the observed correlations between ^{226}Ra and ^{230}Th excesses and $\text{Mg}^\#$ is a coincidence.

Before interpreting these data in terms of melting processes, we examine the possible influence of secondary crustal processes on U-series disequilibrium activity ratios and the effect of ^{226}Ra decay as a function of magma storage time.

4.3.1. Assessing the influence of secondary alteration and crustal assimilation on the U-SERIES data

There are several lines of evidence that suggest that ^{226}Ra , ^{230}Th , and ^{231}Pa excesses generated in our very young axial samples are not a result of secondary processes, such as alteration or assimilation:

1. All of the samples used in this study were fresh, hand-picked glasses and have $^{234}\text{U}/^{238}\text{U}$ activity ratios = 1, indicating minimal posteruption alteration. For submarine basalts, $^{234}\text{U}/^{238}\text{U}$ activity ratios are a sensitive indicator of alteration, as seawater is significantly enriched in ^{234}U relative to ^{238}U ($^{234}\text{U}/^{238}\text{U} = 1.14$; Ku et al., 1977).
2. The Cl/K ratio is a sensitive indicator of assimilation of hydrothermal fluids or hydrothermally altered crust that contains minerals such as barite (eg., Michael and Cornell, 1998). For our samples, Cl/K varies from 0.02 to 0.4 and is not correlated with $\text{Mg}^\#$ (Fig. 12A). While this region of the EPR has extensive hydrothermal venting (Haymon et al., 1991, 1993; Von Damm et al 2000), which involves crustal alteration, there is no significant correlation between Cl/K and $^{226}\text{Ra}/^{230}\text{Th}$ or $^{230}\text{Th}/^{238}\text{U}$ and Cl/K. This lack of correlation between ^{226}Ra and ^{230}Th excesses and Cl/K demonstrates that ^{226}Ra and ^{230}Th excesses are not caused by assimilation of hydrothermally modified material.
3. B isotopes are sensitive indicators of water-rock interaction and assimilation of altered oceanic crust, as there is a large range of variability between unaltered MORB ($d11\text{B} = -5$ to -10), seawater ($d11\text{B} = +40$), and altered crust ($d11\text{B} = +8$). Limited measurements of B isotopes in these samples (Sims et al unpublished data) show that they are in the range of normal MORB, demonstrating that these samples have not assimilated significant amounts of altered oceanic crust.
4. Several studies have investigated the influence of secondary, low-temperature alteration on ^{230}Th excesses and concluded that ^{230}Th excesses are not a result of such processes (Goldstein et al, 1989; Reinitz and Turekian, 1989; Bourdon et al., 2000). Furthermore, it is important to note that Volpe and Goldstein (1993) have also shown that for old, off-axis samples, ^{226}Ra is in equilibrium with ^{230}Th activities, indicating that ^{226}Ra excesses are decaying rather than increasing as the samples age and become altered.

4.3.2. Effect of apatite fractionation on $^{230}\text{Th}/^{238}\text{U}$

Th and U are highly incompatible in most crystallizing phases, and therefore, it is unlikely that crystal fractionation in crustal or subcrustal magma chambers is creating the observed increase in Th excess with decreasing $\text{Mg}^\#$. There is some evidence to suggest that crystallization of apatite during magma differentiation could fractionate U from Th. However, it is unlikely that the large ^{230}Th excesses observed in these samples can be explained by apatite crystallization, particularly since apatite is not on the solidus for these samples. Apatite does not start to crystallize until the P_2O_5 concentration is at ~ 0.5 wt.% in basaltic liquids; our samples have $\text{P}_2\text{O}_5 < 0.25$ wt.%. High F contents in a magma can stabilize the formation of apatite at lower levels of P_2O_5 concentration, but this is also unlikely, as correlations between P_2O_5 and TiO_2 and MgO and P_2O_5 indicate that P was behaving as an incompatible element in this suite of magmas. Furthermore, apatite has a very high $D_{\text{Th}}/D_{\text{U}}$ ratio, and its crystallization in the magmas would drive the liquids toward ^{238}U excesses rather than ^{230}Th excesses, as observed.

4.3.3. Effect of plagioclase fractionation on $^{226}\text{Ra}/^{230}\text{Th}$

Plagioclase contains limited amounts of Ra, but negligible amounts of U and Th (Blundy and Wood, 1994; Cooper et al., 2000). Therefore, in principle, plagioclase fractionation can fractionate Ra from Th, which would change the measured $^{226}\text{Ra}/^{230}\text{Th}$ activity ratio. Crystallization and retention of plagioclase in the axial chamber during magma storage and differentiation could decrease the measured $^{226}\text{Ra}/^{230}\text{Th}$ ratio, as observed. Like Ra, Ba is also an alkaline earth and is thought to be even more compatible than Ra during plagioclase fractionation (Blundy and Wood, 1994; Dunn and Sen, 1994; Cooper et al., 2000). Therefore, Ba/Th can be used to assess the effects of plagioclase fractionation on the measured $^{226}\text{Ra}/^{230}\text{Th}$ ratio. Among our axial 9 to 10°N samples, there is $\sim 20\%$ variation in Ba/Th, with Ba/Th decreasing slightly with decreasing $\text{Mg}^\#$. If this variation is attributed to plagioclase fractionation and one assumes that the crystal/liquid partition coefficient, D_{Ba} , is equal to D_{Ra} for plagioclase/liquid, then the $^{226}\text{Ra}/^{230}\text{Th}$ ratio in the more fractionated samples could be reduced by as much as 20%. This value is half the observed range in ^{226}Ra excess in our samples ($\sim 42\%$). Furthermore, recent evidence indicates that Ra is much less compatible than Ba in plagioclase ($D_{\text{Ba}} > 4 D_{\text{Ra}}$) (Blundy and Wood, 1994; Goldstein et al 1999; Cooper et al 2000). This evidence suggests that the large variation observed in ^{226}Ra excesses cannot be produced by plagioclase fractionation.

4.3.4. Influence of crustal magma storage times on U-SERIES disequilibria

For our axial 9 to 10°N lava suite, there are currently two estimates of magma storage time. These estimates range from < 2 yr, based on crystal growth rates from Kilauea Iki and plagioclase zonation in lavas from the EPR around $9^\circ 31'\text{N}$ (Brophy and Allan, 1993), to as much as 10 ka, based on thermal modeling of a large, hydrothermally cooled AMC (Lister, 1983).

If $^{226}\text{Ra}/^{230}\text{Th}$ is produced by the melting process, then the

large ^{226}Ra excesses measured in these samples limit the crustal magma storage time to be less than or similar to the half-life of ^{226}Ra (1.6 ka). This length of time is small compared to the half-lives of ^{230}Th and ^{231}Pa , indicating that the U-Th and U-Pa disequilibrium activity ratios of these samples have not decayed significantly as a result of magma storage times.

If it is assumed that all our axial lava samples started with the same initial ^{226}Ra ratio and $\text{Mg}^\#$ before differentiation, the correlation between ^{226}Ra excess and $\text{Mg}^\#$ for this sample suite can, in principle, be used to estimate the time scales of crustal magma differentiation. Using a linear relationship between magma storage time and the extent of crystallization, magma storage times can be determined by extrapolation of the correlation between ^{226}Ra excess and $\text{Mg}^\#$ back to an assumed primitive magma composition ($\text{Mg}^\# 71$). For our entire axial 9 to 10°N data set, we calculate an initial ^{226}Ra excess of 3.1 and magma storage times of ~ 300 to 2000 yr for a closed-system fractional crystallization model and ~ 150 to 900 yr for a steady-state, open-system magma storage model (e.g., Pyle, 1992, 1994; Condomines, 1994). Note that if crystallization rates are nonlinear and increase with extent of crystallization, then modeled magma storage times will be longer than those determined for the linear crystallization rate model. On the other hand, if ^{226}Ra excesses have been reduced by plagioclase crystallization, magma storage times would be smaller than estimated.

Finally, it is important to note that it is a primary assumption for the above-modeled crustal magma storage times that all primary melts started with uniform ^{226}Ra and $\text{Mg}^\#$. The observation that ^{230}Th excesses increase with decreasing $\text{Mg}^\#$ suggests that these lavas started out with different initial ^{230}Th excesses and, by inference, different ^{226}Ra excesses. If some or all of the variation is due to the melting process, then the crustal magma storage times would be substantially smaller than calculated. The possibility that the observed variations in ^{230}Th and ^{226}Ra excesses (and $\text{Mg}^\#$) are due to the melt generation and transport processes is discussed in detail in the following section.

4.4. U-Series Constraints on Melting Process

A fundamental feature of our data on axial 9 to 10°N lavas is that $^{230}\text{Th}/^{238}\text{U}$ and $^{226}\text{Ra}/^{230}\text{Th}$ are variable and negatively correlated. While other MORB data have shown similar trends between ^{226}Ra and ^{230}Th excesses, a lack of constraints on the mantle source composition and the large uncertainties in sample eruption ages and magma storage times have made it difficult to interpret the ^{226}Ra data in terms of melting processes (Volpe and Goldstein, 1993; Lundstrom et al., 1998, 1999). The significance of the observed negative correlation between ^{226}Ra and ^{230}Th in the axial 9 to 10°N data is that (a) all of these samples are known to have erupted within or just outside the axial summit trough, and their ages are demonstrably very young; (b) these lavas come from a homogeneous mantle source, as indicated by their Sr, Nd, Hf, and Pb isotope ratios; and (c) there is considerable evidence precluding the influence of water-rock interaction, assimilation of altered crust, or secondary minerals or crystallization on their measured ^{230}Th and ^{226}Ra excesses.

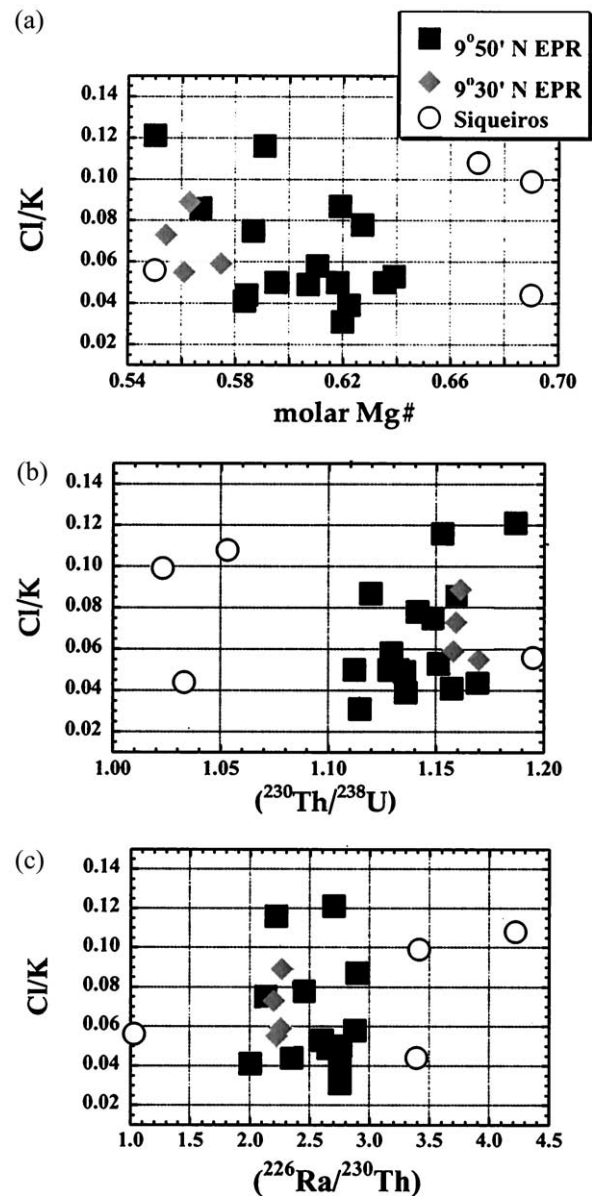


Fig. 12. (A) $\text{Mg}^\#$ vs. Cl/K, (B) ^{230}Th excess vs. Cl/K, and (C) ^{226}Ra excess vs. Cl/K for the axial 9 to 10°N and Siqueiros Transform samples. EPR = East Pacific Rise.

Understanding the large ^{230}Th , ^{231}Pa , and ^{226}Ra excesses measured in our sample suite require models that incorporate the time scales of melt generation and transport. However, neither dynamic nor pure reactive porous flow models can produce the observed negative correlation between ^{230}Th and ^{226}Ra excesses. Melts produced by dynamic melting have positively correlated ^{230}Th and ^{226}Ra excesses, whereas melts produced by reactive porous flow to shallow levels would have no ^{230}Th excesses, since $D_{\text{U}} < D_{\text{Th}}$ in the shallow mantle.

The negative correlation of ^{226}Ra and ^{230}Th excesses requires that two different processes generate these excesses in the melting column. This is possible if two different pathways exist for moving melt to the surface, with one pathway being reactive transport through low-porosity matrix and the other

being nonreactive transport through high-porosity channels (Iwamori, 1993; Kelemen et al., 1997; Sims et al., 1998; Lundstrom et al., 2000; Jull et al. submitted). The high-porosity pathways are envisaged to result from a “reactive infiltration instability,” resulting in the localization of initially diffuse melt flow due to increased solubility of pyroxene at shallow depths (Kelemen et al., 1997; Spiegelman et al., 2001). Both Lundstrom et al. (2000) and Jull et al. (submitted) have modeled the consequence of this “two-porosity” melt transport mode on U-series disequilibria and trace element systematics. In these models, they assumed that melt is transferred from the low-porosity interchannel region to the high-porosity channels as it moves upward through the melting column. The results of Jull et al.’s (submitted) modeling show that these 9 to 10°N EPR data can be explained by a two-porosity model if ~60% of the total melt flux travels through the low-porosity region, and ~40% travels through high-porosity channels that occupy <10% of the melting region. Mixing of melt from these two different pathways at the top of the melt column can produce the observed negative slope and magnitude of ^{226}Ra and ^{230}Th excesses, as well as the trace element systematics in MORB. Furthermore, Jull et al. (submitted) show that increased efficiency of melt transfer in the shallow mantle to the high-porosity channels can account for the depleted trace element concentrations observed in some abyssal peridotites and explain the lack of orthopyroxene saturation in MORB. On the basis of the numerical results of Jull et al. (submitted), we infer that melt transport beneath the axial 9 to 10°N area of the EPR occurs via both low-porosity reactive transport and high-porosity nonreactive transport and that the erupted magmas represent mixtures of melts from these different regions. While not modeled by Jull et al. (submitted), we suggest that the relatively constant ^{231}Pa excesses in our samples are consistent with this melt transport scenario. A constant ^{231}Pa excess with increasing ^{230}Th excess is because Pa and Th maintain $D_{\text{Pa}} < D_{\text{Th}}$ at shallow levels in the mantle, and the half-life of ^{231}Pa is long compared to that of ^{226}Ra . As a result, ^{231}Pa is maintained along both the low-porosity pathways and the high-porosity channels.

The major and trace element compositions of our samples also support the hypothesis that these lavas represent mixtures of melts equilibrated at different depths. This hypothesis is consistent with our previous observations of Sm/Nd and U-Th disequilibria in axial basalts from the Juan de Fuca and Gorda ridges, which we interpreted as mixing of large and small degree partial melts (Sims et al., 1995). For the 9°N EPR samples, we suggest that deep melts equilibrated with less depleted lherzolite near the base of the melting column, and shallow melts equilibrated with highly depleted harzburgite near the top. Although the range of variability in the major and trace element concentrations is limited compared to the analytical uncertainties, ^{230}Th excesses tend to be inversely correlated with the “degree of partial melting” as inferred from La/Yb, Sm/Nd, and Na_g . In contrast, ^{226}Ra excesses tend to increase with the inferred “degree of melting,” opposite to the trend expected for fractional melting. As discussed below, these trends are better correlated and greatly extended when data from very depleted MORB from the Siqueiros Transform are also considered.

Finally, the correlation observed between ^{230}Th and ^{226}Ra

excesses and $\text{Mg}^\#$ of these samples can also be explained by the mixing of deep and shallow melts. Because primary melts generated at variable depths have different compositions that evolve along distinct liquid lines of descent, the differences in crystallization that occur during cooling results in a large range of $\text{Mg}^\#$ for a given temperature. This is illustrated in Figure 13, which shows the predicted $\text{Mg}^\#$ for cooling and crystallization from 1350 to 1200°C of three different calculated melt compositions from the bottom, middle, and top of the melt column (calculated from Gaetani and Watson, 2002). Because the shallow melt equilibrated with depleted peridotite, it starts with a higher $\text{Mg}^\#$ compared to the deeper melt. Also, the shallow melt is closer to its liquidus conditions at the base of the crust; as a result, it crystallizes less olivine and evolves to a higher $\text{Mg}^\#$ over a given temperature interval. The deeper melt is well below its liquidus temperature at the base of the crust, starts to crystallize olivine substantially earlier, and eventually crystallizes clinopyroxene; as a result of crystallizing both more olivine and clinopyroxene, this deeper melt evolves to a lower $\text{Mg}^\#$ over the same temperature interval. If it is assumed that the time scale of crystallization is short compared to the half-lives of ^{230}Th and ^{226}Ra , then these differences in model $\text{Mg}^\#$ values, for a given temperature of final crystallization, when compared with the ^{230}Th and ^{226}Ra excesses of the Siqueiros E-MORB, D-MORB, and the average 9 to 10°N EPR N-MORB, produce trends that are similar to the correlations between $\text{Mg}^\#$ and ^{230}Th excess and ^{226}Ra excess observed in the EPR data (Figs. 13B and 13C). The ability of this model to reproduce these correlations between $\text{Mg}^\#$ and ^{230}Th and ^{226}Ra excesses suggests that (a) not all MORBs start with the same primary $\text{Mg}^\#$, (b) the average time scale of crystallization is short compared to the half-life of ^{226}Ra , and (c) the long-held observation that the most light rare earth element-enriched MORB samples are also the ones with the lowest $\text{Mg}^\#$ (Bryan et al., 1979, 1981; Perfit et al., 1994) can be explained by a simple and self-consistent model of mixing of melts taken from different depths.

5. COMPARISON BETWEEN AXIAL 9 TO 10°N LAVAS AND SIQUEIROS TRANSFORM SAMPLES

Samples collected using *Alvin* and by dredge from the Siqueiros Transform at 8°20'N constitute an important data set, as they represent rocks from the first second-order discontinuity south of the EPR segment where our axial lava suite was collected. The Siqueiros samples form both depleted and enriched end-members of the global correlation between ^{230}Th and ^{226}Ra excesses in MORB.

The Siqueiros Transform is a left-lateral offset along the EPR with a displacement of 140 km, along which are four intratransform spreading centers (Fornari et al., 1989). The Siqueiros samples analyzed in this study and by Lundstrom et al. (1998), Perfit et al. (1996), and Natland (1989) are petrologically and compositionally diverse. Glass compositions range from incompatible element-depleted “picritic” basalts, called “D-MORBs,” containing >9 wt.% MgO, to slightly nepheline-normative alkali basalts, termed “E-MORBs.” The D-MORBs are very young-appearing, glassy basalts collected by *Alvin* from a site in the middle of the A-B transform (Perfit et al., 1996). They represent near-primary, high-MgO melts (10

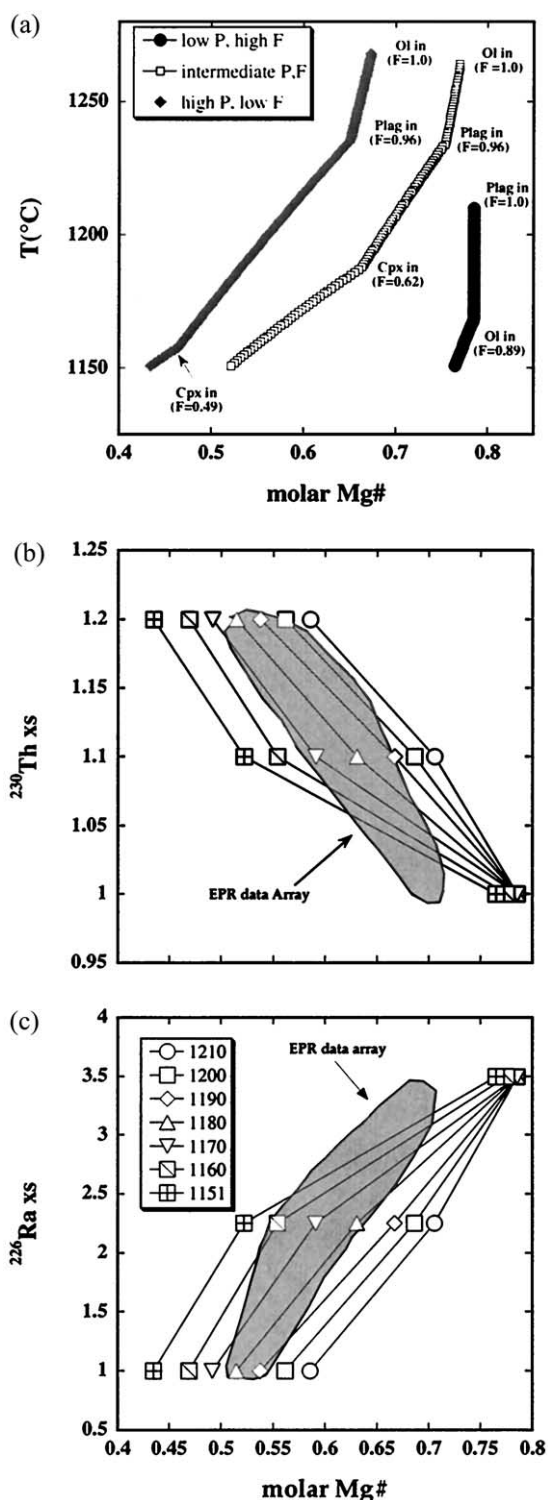


Fig. 13. (A) Modeled Mg[#] for cooling and crystallization, from 1350 to 1150°C at 0.2 GPa, of three different near-fractional peridotite melts from the bottom (20 kb; *f* = 0.01), middle (10 kb; *f* = 0.077), and top (3 kb; *f* = 0.140) of the melt column. Initial melt compositions were taken from Table 1 of Gaetani and Watson (2002), which were calculated using the partial melting model of Kinzler (1997); for the fractional crystallization calculations, we use Weaver and Langmuir's (1990) fractional crystallization model. The lines start when a phase begins to precipitate; each inflection shows the beginning of a new crystallizing phase with the remaining melt fraction (*F*) indicated. The

wt.% MgO and Mg[#] ~ 69 to 72 in glasses), are highly depleted in incompatible trace elements, and have high ²²⁶Ra and low ²³⁰Th excesses. The E-MORBs are dredge samples that were collected from the ridge-transform intersection. Siqueiros E-MORBs are evolved (Mg[#] < 60), highly enriched in incompatible trace elements, and have low ²²⁶Ra and high ²³⁰Th excesses.

The Siqueiros data extend the correlations observed between Mg[#] and ²²⁶Ra and ²³⁰Th excesses and between melt-depletion parameters such as La/Yb, Na₈, and alpha Sm/Nd and ²²⁶Ra and ²³⁰Th excesses (Fig. 9). While Siqueiros D-type lavas provide a definitive end-member in this correlation, the initial ²²⁶Ra excesses in Siqueiros E-type lavas (which represent the high-²³⁰Th, low-²²⁶Ra end-member) are uncertain, as these are dredge samples of unknown age and are in equilibrium with respect to ²²⁶Ra. In fact, the E-MORB sample used also has lower ²³¹Pa/²³⁵U and ²³⁰Th/²³⁸U than would be predicted by extension of the different data correlations, and has been age corrected (Lundstrom et al., 1999), based on Goldstein et al.'s (1992, 1993, 1994) approach and the extents of U-Th and U-Pa disequilibrium measured in the near-axis E-MORB sample (R54-2), from near the 9°37'N DEVAL, which shows a significant ²²⁶Ra excess (Volpe and Goldstein, 1993).

Limited measurements of Nd and Sr isotopes have previously shown that the Siqueiros D-MORB and E-MORB lavas

shallow melt, which equilibrated with depleted peridotite, starts with a higher Mg[#], crystallizes less olivine, and therefore equilibrates to a higher Mg[#] at a given temperature, whereas the deeper melt is more iron rich, starts to crystallize olivine immediately, and finally crystallizes clinopyroxene, therefore evolving to a lower Mg[#] over the same temperature interval. With polybaric melting, the shallow, large degree melt has more CaO and Al₂O₃ and therefore crystallizes plagioclase before olivine (see Gaetani and Watson, 2002, or Kinzler, 1997, for details). These calculations use the end-member melts from Gaetani and Watson (2002) that result in a range of calculated Mg[#] values larger than observed in the actual East Pacific Rise (EPR) data. (Despite the large range in Mg[#] of the end-member melts we used, the forsterite content of residual mantle olivines in equilibrium with these end-member melts ranges from 0.90 for the deep melt to 0.91 for the shallow melt, well within the observed variation of olivine compositions in abyssal peridotites and other residual mantle samples). If the polybaric melts were more similar in their composition, crystallizing along parallel, nearly overlapping trends resembling a single liquid line of descent, the deeper melt would still start out richer in both Mg and Fe and with a lower Mg[#] than the shallow melt. Because of its relatively high normative olivine content, compared to the shallow melt, the deeper melt would therefore crystallize more olivine over the same temperature interval and evolve to a lower Mg[#] than the shallow melt. (B) Model Mg[#] vs. ²³⁰Th excess for different final temperatures of crystallizing melts, which started at 1350°C using the trends in (A) and assuming that low-*P* melts had no ²³⁰Th excess, intermediate-*P* melts had ²³⁰Th excess = 1.1, and high-*P* melts had ²³⁰Th excess = 1.2. These choices for Th excess are consistent with a change in residual mineralogy from garnet-to-spinel peridotite and are guided by the observed Siqueiros and 9 to 10°N EPR data (see, e.g., Fig. 8). These model trends between Mg[#] and ²³⁰Th excess assume that time scale of crystallization is short relative to the half-life of ²³⁰Th. (C) Model Mg[#] vs. ²²⁶Ra excess for different final temperatures of crystallizing melts, which started at 1350°C using the trends in (A) and assuming that low-*P* melts had ²²⁶Ra excess = 3.5, intermediate-*P* melts had ²²⁶Ra excess = 2.3, and high-*P* melts had ²²⁶Ra excess = 1.0. These choices for Ra excess are consistent and guided by the observed values in the Siqueiros and 9 to 10°N EPR data (see, e.g., Fig. 8). These model trends between Mg[#] and ²²⁶Ra excess assume that time scale of crystallization is short relative to the half-life of ²²⁶Ra.

come from isotopically distinct sources (Natland, 1989; Perfit et al., 1996). Here, we report additional measurements of Nd, Hf, Sr, and Pb isotopes for Siqueiros lava samples (Table 2 and Figs. 2 to 4 and 10A to 10D). These data show that the D-MORBs have Nd, Hf, Sr, and $^{208}\text{Pb}/^{206}\text{Pb}$ isotopic ratios that are similar to our axial 9 to 10°N lava suite, whereas the one analyzed Siqueiros E-MORB sample clearly comes from an isotopically distinct and more enriched source. This would suggest that melting and melt transport processes control the variation observed in ^{230}Th and ^{226}Ra excesses for our both our axial 9 to 10°N suite and the Siqueiros D-MORB but that the variation observed in the ^{230}Th excesses for the E-MORB lava might be attributable to melting of a chemically distinct source.

The Pb isotopic data for the Siqueiros samples, considered independently of our axial 9 to 10°N data, show a single array, which if interpreted in terms of a single- or two-stage Pb evolution model indicates that all the Siqueiros samples come from a source with a relatively constant Th/U ratio and variable U/Pb and Th/Pb ratios. However, the Siqueiros trend for the thorogenic and uranium Pb isotopes, $^{208}\text{Pb}/^{204}\text{Pb}$ vs. $^{206}\text{Pb}/^{204}\text{Pb}$, is different from the trend formed by our axial 9 to 10°N data. On the basis of these data, one could infer that Th/U in the Siqueiros source is different from Th/U in the axial 9 to 10°N source. However, as indicated by the $^{208}\text{Pb}/^{206}\text{Pb}$ ratio of these samples, the range in Th/U inferred from the Pb isotopes for both the D-MORBs and the axial 9 to 10°N N-MORBs is much smaller than the range in Th/U observed within the combined Siqueiros and axial 9 to 10°N data sets. This suggests that most of the variability in Th/U in this region must be due to elemental fractionation during melting and melt transport rather than source composition.

6. CONCLUSIONS

1. In very young lava samples collected using *Alvin* from within the axial trough between $9^\circ28'$ and $9^\circ52'\text{N}$, ^{230}Th excesses and ^{226}Ra excesses are inversely correlated and vary with the major and trace element composition
2. These variations are not due to crustal processes such as assimilation of altered material or crystallization of apatite or plagioclase
3. Axial 9 to 10°N samples have constant $^{143}\text{Nd}/^{144}\text{Nd}$, $^{87}\text{Sr}/^{86}\text{Sr}$, $^{176}\text{Hf}/^{177}\text{Hf}$, and $^{208}\text{Pb}/^{206}\text{Pb}$ isotopic compositions. Siqueiros D-MORBs have $^{143}\text{Nd}/^{144}\text{Nd}$, $^{87}\text{Sr}/^{86}\text{Sr}$, $^{176}\text{Hf}/^{177}\text{Hf}$, and $^{208}\text{Pb}/^{206}\text{Pb}$ isotopic ratios that are the same as axial 9 to 10°N lavas. This observation suggests that the measured variations of Th/U, ^{230}Th , and ^{226}Ra excesses and major and trace element compositions in both the axial 9 to 10°N and Siqueiros D-MORB samples are not due to mixing of variable source compositions.
4. The one Siqueiros E-MORB sample analyzed clearly comes from an isotopically distinct and more enriched source than the axial 9 to 10°N samples and the Siqueiros D-MORB. The chemical differences between the Siqueiros E-MORB and the other samples may be due in part to melting of a chemically and isotopically distinct source.
5. The observed correlations between ^{230}Th excess, ^{226}Ra excess, $\text{Mg}^\#$, La/Yb, alpha Sm/Nd, and Na_8 suggest mixing of two types of melt: one having a high ^{226}Ra excess and the other a high ^{230}Th excess. In this context, the high ^{226}Ra

component preserves characteristics indicative of equilibration with highly depleted, residual harzburgite in the uppermost (spinel facies) mantle, whereas the high ^{230}Th component equilibrated with deeper, less depleted garnet peridotites. This suggests that melt transport requires some reactive process to produce the low- ^{230}Th , high- ^{226}Ra component at shallow depths. Furthermore, it would appear that the low ^{226}Ra excess in the high ^{230}Th component reflects ^{226}Ra decay before eruption (e.g., during magma transport and/or storage).

Acknowledgments—The authors thank Mark Reagan and Glenn Gaetani for invaluable discussions and Craig Lundstrom, Simon Turner, Tim Elliott, Haibou Zou, and Ken Rubin for constructive reviews. Support for this research was provided by a Woods Hole Oceanographic Institution postdoctoral fellowship (K. W. Sims); National Science Foundation grants OCE-9730967 (K. W. Sims), OCE-9100503 (M. R. Perfit and D. J. Fornari), OCE-9402360 and OCE-9403773 (M. R. Perfit), and OCE-9408904 and OCE-9912072 (D. J. Fornari); and from Basic Energy Science, U.S. Department of Energy (M. T. Murrell and S. J. Goldstein).

Associate editor: F. A. Frey

REFERENCES

- Bateman H. (1910) Solution of a system of partial differential equations occurring in the theory of radioactive transformations. *Proc. Cambridge Philos. Soc.* **15**, 423.
- Batiza R. and Niu Y. (1992) Petrology and magma chamber processes at the East Pacific Rise— $9^\circ30'\text{N}$. *J. Geophys. Res.* **97**, 6779–6797.
- Beattie P. (1993a) Uranium-thorium disequilibrium and partitioning on melting of garnet peridotite. *Nature* **363**, 63–65.
- Beattie P. (1993b) The generation of uranium series disequilibria by partial melting of spinel peridotite: Constraints from partitioning studies. *Earth Planet. Sci. Lett.* **117**, 379–391.
- Ben Othman D. and Allegre C. J. (1990) U-Th isotopic systematics at 13°N East Pacific Ridge segment. *Earth Planet. Sci. Lett.* **98**, 129–137.
- Blichert-Toft J., Chauvel C., and Albarède F. (1997) Separation of Hf and Lu for high-precision isotope analysis of rock samples by magnetic sector-multiple collector ICP-MS. *Contrib. Mineral. Petrol.* **127**, 248–260.
- Blundy J. and Wood B. (1994) Prediction of crystal-melt partition coefficients from elastic moduli. *Nature* **372**, 452–454.
- Bourdon B., Zindler A., Elliott T., and Langmuir C. H. (1996) Constraints on mantle melting at mid-ocean ridges from global ^{238}U - ^{230}Th disequilibrium data. *Nature* **384**, 231–235.
- Bourdon B., Goldstein S. J., Murrell M. T., Bourles D., Langmuir C. H. (2000) Evidence from ^{10}Be and U-series disequilibria on possible contamination of mid-ocean ridge basalt glasses by sedimentary material. *Geochem. Geophys. Geosys.* **1** (paper number 2000GC000047).
- Boudier F. and Nicolas A. (1995) Nature of the Moho transition zone in the Oman ophiolite. *J. Petrol.* **36**, 777–796.
- Brophy J. G., Allan J. F. (1993) Textural and mineralogic studies of plagioclase phenocrysts from ODP Leg 142, Site 864A: Implications for magmatic processes beneath the East Pacific Rise (EPR) $9^\circ30'\text{N}$. *Trans. Am. Geophys. Union*, Fall Meeting Suppl., **74**, 644.
- Bryan W. B., Thompson G., and Michael P. J. (1979) Compositional variation in a steady-state zoned magma chamber: Mid-Atlantic Ridge at $36^\circ50'\text{N}$. *Tectonophysics* **55**, 63–85.
- Bryan W. B., Thompson G., and Ludden J. N. (1981) Compositional variation in normal mid-ocean ridge basalts from 22°N – 25°N : Mid-Atlantic Ridge and Kane Fracture Zone. *J. Geophys. Res.* **86**, 11815–11836.
- Carbotte S. M. and Macdonald K. C. (1992) East Pacific Rise 8° – $10^\circ30'\text{N}$: Evolution of ridge segments and discontinuities from Sea-MARC II and three-dimensional magnetic studies. *J. Geophys. Res.* **97**, 6959–6982.

- Cochran J. R., Fornari D. J., Coakley B. J., Herr R., and Tivey M. A. (1999) Continuous near-bottom gravity measurements made with a BGM-3 gravimeter in DSV Alvin on the East Pacific Rise crest near 9°30'N and 9°50'N. *J. Geophys. Res.* **104**, 10841–10861.
- Condomines M. (1994) Comment on: "The volume and residence time of magma beneath active volcanoes determined by decay-series disequilibria methods." *Earth Planet. Sci. Lett.* **122**, 251–255.
- Condomines M. and Sigmarsson O. (2000) ^{238}U - ^{230}Th disequilibria and mantle melting processes: A discussion. *Chem. Geol.* **162**, 95–104.
- Condomines M., Hemmond C., and Allegre C. J. (1988) U-Th-R a disequilibria and magmatic processes. *Earth Planet. Sci. Lett.* **90**, 243–263.
- Cooper K. M., Reid M. R., Murrell M. T., and Clague D. A. (2000) Crystal and magma residence at Kilauea volcano, Hawaii: ^{230}Th - ^{226}Ra dating of the 1955 east rift eruption. *Earth Planet. Sci. Lett.* **5692**, 1–16.
- DePaolo D. J. (1988) *Neodymium Isotope Geochemistry*. Springer-Verlag, New York.
- DePaolo D. J. (1996) High-frequency isotopic variations in the Mauna Kea tholeiitic basalt sequence: Melt zone dispersivity and chromatography. *J. Geophys. Res.* **101**, 11855–11864.
- Detrick R. S., Buhl P., Vera E., Orcutt J., Madsen J., and Brocher T. (1987) Multi-channel seismic imaging of a crustal magma chamber along the East Pacific Rise. *Nature* **326**, 35–41.
- Dick H. J. B., Fisher R. L., and Bryan W. B. (1984) Mineralogical variability of the uppermost mantle along mid-ocean ridges. *Earth Planet. Sci. Lett.* **69**, 88–106.
- Dunn T. and Sen C. (1994) Mineral/matrix partition coefficients for orthopyroxene, plagioclase, and olivine in basaltic to andesitic system: A combined analytical and experimental study. *Geochim. Cosmochim. Acta* **58**, 717–733.
- Dunn R. A., Toomey D. R., and Solomon S. C. (2000) Three dimensional seismic structure and physical properties of the crust and shallow mantle beneath the East Pacific Rise at 9°30'N. *J. Geophys. Res.* **105**, 23537–23555.
- Elliott T., Zindler A., and Bourdon B. (1999) Exploring the kappa conundrum: The role of recycling in the lead isotope evolution of the mantle. *Earth Planet. Sci. Lett.* **169**, 129–145.
- Fornari D. J., Gallo D. G., Edwards M. H., Madsen J. A., Perfit M. R., and Shor A. N. (1989) Structure and topography of the Siqueiros Transform fault system: Evidence for the development of intra-transform spreading centers. *Mar. Geophys. Res.* **11**, 263–299.
- Fornari D., Haymon R., Perfit M., Gregg T. K. P., and Edwards M. H. (1998) Axial summit trough of the East Pacific Rise, 9°–10°N: Geological characteristics and evolution of the axial zone on fast spreading mid-ocean ridges. *J. Geophys. Res.* **103**, 9827–9855.
- Forsyth D. W. 1992 Geophysical constraints on mantle flow and melt generation beneath mid-ocean ridges. In *Mantle Flow and Melt Generation at Mid-Ocean Ridges* (eds. J. P. Morgan, D. K. Blackman, and J. M. Sinton). *Geophys. Monogr.* **71**, 1–67. American Geophysical Union, Washington, DC.
- Galer S. J. G. and O'Nions R. K. (1985) Residence time of thorium, uranium and lead in the mantle with implications for mantle convection. *Nature* **316**, 778–782.
- Galer S. J. G., Abouchami W., and Macdougall J. D. (2000) Pb isotopic evidence for coherent mantle domains beneath the East Pacific Rise. *J. Conf. Abst.* **5**, (2) 421 (abstract).
- Gaetani G. A. and Watson E. B. (2002) Modeling the major-element evolution of olivine-hosted melt inclusions. *Chem. Geol.* **183**, 25–41.
- Goldstein S. J., Murrell M. T., and Janecky D. R. (1989) Th and U isotopic systematics of basalts from the Juan de Fuca and Gorda Ridges by mass spectrometry. *Earth Planet. Sci. Lett.* **96**, 134–146.
- Goldstein S. J., Murrell M. T., Janecky D. R., Delaney J. R., and Clague D. A. (1992) Geochronology and petrogenesis of MORB from the Juan de Fuca and Gorda ridges by ^{238}U - ^{230}Th disequilibrium. *Earth Planet. Sci. Lett.* **107**, 25–41.
- Goldstein S. J., Murrell M. T., and Williams R. W. (1993) ^{231}Pa and ^{230}Th chronology of mid-ocean ridge basalts. *Earth Planet. Sci. Lett.* **115**, 151–160.
- Goldstein S. J., Perfit M. R., Batiza R., Fornari D. J., and Murrell M. T. (1994) Off-axis volcanism at the East Pacific Rise detected by uranium-series dating of basalts. *Nature* **367**, 157–159.
- Goldstein S. J., Sims K. W., Cooper K., Murrell M. T., Nunn A. J. (1999) Evidence for radium-barium fractionation in MORB plagioclase: Implications for chronology and mantle melting. Ninth Annual V. M. Goldschmidt Conference, Cambridge, MA.
- Grove T. L. and Bryan W. B. (1983) Fractionation of pyroxene-phyric MORB at low pressures: An experimental study. *Contrib. Mineral. Petrol.* **84**, 293–309.
- Haymon R. M., Fornari D. J., Edwards M. H., Carbotte S. C., Wright D., and Macdonald K. C. (1991) Hydrothermal vent distribution along the East Pacific Rise Crest (9°09'–54'N) and its relationship to magmatic and tectonic processes on fast-spreading mid-ocean ridges. *Earth Planet. Sci. Lett.* **104**, 513–534.
- Haymon R., Fornari D. J., Von Damm K., Lilley M., Perfit M., Edmond J., Shank III W. C., Lutz R., Grebeier J., Carbotte S., Wright D., McLaughlin E., Smith M., Beedle N., and Olson E. (1993) Volcanic eruption of the mid-ocean ridge along the East Pacific at 9°45'–52'N: I. Direct submersible observation of sea floor phenomena associated with an eruption event in April, 1991. *Earth Planet. Sci. Lett.* **119**, 85–101.
- Holmes A. (1946) An estimate of the age of the Earth. *Nature* **157**, 680–684.
- Houtermans F. G. (1946) Die Isotopenhäufigkeiten im natürlichen Blei und das Alter des Urans. *Naturwissenschaften* **33**, 185–186.
- Iwamori H. (1993) A model for disequilibrium mantle melting incorporating melt transport by porous and channel flows. *Nature* **366**, 734–737.
- Iwamori H. (1994) ^{238}U - ^{230}Th - ^{226}Ra and ^{235}U - ^{231}Pa disequilibria produced by mantle melting with porous and channel flows. *Earth Planet. Sci. Lett.* **125**, 1016.
- Johnson K. T. M. and Dick H. J. B. (1992) Open system melting and temporal and spatial variation of peridotite and basalt at the Atlantis II fracture zone. *J. Geophys. Res.* **97**, 9219–9241.
- Johnson K. T. M., Dick H. J. B., and Shimizu N. (1990) Melting in the oceanic upper mantle: An ion microprobe study of diopsides in abyssal peridotites. *J. Geophys. Res.* **95**, 2661–2678.
- Jull M. Kelemen P. B., Sims K. W. (submitted) Consequences of diffuse and channeled porous melt migration on U Series disequilibria. *Geochim. Cosmochim. Acta*.
- Kelemen P. B., Shimizu N., and Salters V. J. M. (1995) Extraction of mid-ocean-ridge basalt from the upwelling mantle by focused flow of melt in dunite channels. *Nature* **375**, 747–753.
- Kelemen P. B., Hirth G., Shimizu N., Spiegelman M., and Dick H. J. B. (1997) A review of melt migration processes in the adiabatically upwelling mantle beneath oceanic spreading ridges. *Philos. Trans. R. Soc. London, Ser. A* **355**, 1–35.
- Ken G. M., Harding A. J., and Orcutt J. A. (1990) Evidence for a smaller magma chamber beneath the East Pacific Rise at 9°30'N. *Nature* **344**, 650–653.
- Kinzler R. J. (1997) Melting of mantle peridotite at pressures approaching the spinel to garnet transition: Application to mid-ocean ridge basalt petrogenesis. *J. Geophys. Res.* **102**, 853–874.
- Klein E. M. and Langmuir C. H. (1987) Global correlations of ocean ridge basalt chemistry with axial depth and crustal thickness. *J. Geophys. Res.* **92**, 8089.
- Ku T. -L., Knauss K. G., and Mathieu G. G. (1977) Uranium in open ocean: Concentration and isotopic composition. *Deep Sea Res.* **24**, 1005–1017.
- Landwehr D., Blundy J., Chamorro-Perez E. M., Hill E., and Wood B. (2001) U-series disequilibria generated by partial melting of spinel lherzolite. *Earth Planet. Sci. Lett.* **188**, 329–348.
- Langmuir C. H., Bender J. F., Bence A. E., Hanson G. N., and Taylor S. R. (1977) Petrogenesis of basalts from the FAMOUS area: Mid-Atlantic Ridge. *Earth Planet. Sci. Lett.* **36**, 133–156.
- Langmuir C. H., Bender J. F., and Batiza R. (1986) Petrological segmentation of the East Pacific Rise, 5°30'–14°30'N. *Nature* **322**, 422–429.
- Langmuir C. H., Klein E. M., Plank T. M. 1992 Petrological systematics of mid-ocean ridge basalts: Constraints on melt generation beneath ocean ridges. In *Mantle Flow and Melt Generation at Mid-Ocean Ridges* (eds. J. P. Morgan, D. K. Blackman, and J. M. Sinton). *Geophys. Monogr.* **71**, 1–67. American Geophysical Union, Washington, DC.

- LaTourrette T. Z. and Burnett D. S. (1992) Experimental determination of U and Th during partitioning between clinopyroxene and natural and synthetic basalt liquid. *Earth Planet. Sci. Lett.* **110**, 227–244.
- LaTourrette T. Z., Kennedy A. K., and Wasserburg G. J. (1993) U-Th fractionation by garnet—Evidence for a deep source and rapid rise by oceanic basalts. *Science* **261**, 739–742.
- Layne G. D. and Sims K. W. (2000) Secondary ion mass spectrometry for the measurement of $^{232}\text{Th}/^{230}\text{Th}$ in volcanic rocks. *Int. J. Mass Spectrom.* **203**, 1–3, 187–198.
- Lister C. R. B. (1983) On the intermittency and crystallization mechanisms of sub-seafloor magma chambers. *Geophys. J. R. Astr. Soc.* **73**, 351–365.
- Lundstrom C. C., Gill J., Williams Q., and Perfit M. R. (1995) Mantle melting and basalt extraction by equilibrium porous flow. *Science* **270**, 1958–1961.
- Lundstrom C. C., Gill J., Williams Q., and Hanan B. B. (1998) Investigating solid mantle upwelling rates beneath mid-ocean ridges using U-series disequilibria. II. A local study at 33°S MAR. *Earth Planet. Sci. Lett.* **157**, 167–181.
- Lundstrom C. C., Sampson D. E., Perfit M. R., Gill J., and Williams Q. (1999) Insights into mid-ocean ridge basalt petrogenesis: U-series disequilibria from the Siqueiros Transform, Lamont Seamounts, and East Pacific Rise. *J. Geophys. Res.* **104**, 13035–13048.
- Lundstrom C. C., Williams Q., and Gill J. (2000) A geochemically consistent hypothesis for MORB generation. *Chem. Geol.* **162**, 105–126.
- McKenzie D. (1984) The generation and compaction of partially molten rock. *J. Petrol.* **25**, 713–765.
- McKenzie D. (1985) ^{230}Th - ^{238}U disequilibrium and the melting processes beneath ridge axes. *Earth Planet. Sci. Lett.* **72**, 149–157.
- McKenzie D. and Bickle M. J. (1988) The volume and composition of melt generated by extension of the lithosphere. *J. Petrol.* **29**, 625–679.
- Michael P. J. and Cornell W. C. (1998) Influence of spreading rate and magma supply on crystallization and assimilation beneath mid-ocean ridges: Evidence from chlorine and major-element chemistry of mid-ocean ridge basalts. *J. Geophys. Res.* **103**, 18325–18356.
- Natland J. H. (1989) Partial melting of lithologically heterogeneous mantle: Inferences from crystallization histories of magnesian abyssal tholeiites from the Siqueiros Fracture Zone. In *Magmatism in the Ocean Basins* (eds. A. D. Saunders and M. J. Norry). *Geol. Soc. London Spec. Pub.* **42**, 41–70.
- Navo O. and Stolper E. (1987) Geochemical consequences of melt percolation: The upper mantle as a chromatographic column. *J. Geol.* **95**, 384–392.
- Nicholas A. (1986) A melt extraction model based on structural studies in mantle peridotites. *J. Petrol.* **27**, 999–1022.
- Niu Y. (1997) Mantle melting and melt extraction processes beneath spreading ridges: Evidence from abyssal peridotites. *J. Petrol.* **38**, 1047–1074.
- O'Hara M. J. (1968) Are any ocean floor basalts primary? *Nature* **220**, 683–686.
- Perfit M. R., Smith M. C., Fornari D. J., Batiza R., and Edwards M. H. (1992) Submersible transects across the East Pacific Rise crest and upper-flanks 9°31'–32°N: 2. Small scale spatial variations in lava geochemistry and implications for temporal variability. *Eos: Trans. Am. Geophys. Union* **73**, 525.
- Perfit M., Fornari D., Smith M., Bender J., Langmuir C., and Haymon R. (1994) Small-scale spatial and temporal variations in MORB geochemistry and implications for ridge crest magmatic processes. *Geology* **22**, 375–379.
- Perfit M. R., Fornari D. J., Ridley W. I., Kirk P. D., Casy J., Kastens K. A., Reynolds J. R., Edwards M., Desonie D., Shuster R., and Parris S. (1996) Recent volcanism in the Siqueiros Transform fault: picritic basalts and implications for MORB magma genesis. *Earth Planet. Sci. Lett.* **141**, 61–73.
- Perfit M. R. and Chadwick Jr. W. W. (1998) Magmatism at mid-ocean ridges: Constraints from volcanological and geochemical investigations. *Faulting and Magmatism at Mid-Ocean Ridges*. In: (eds. W. R. Buck, P. Delaney, J. A. Karson, and Y. Lababril). American Geophysical Union, Washington, DC, pp. 41–70.
- Pickett D. A., Murrell M. T., and Williams R. W. (1996) Determination of femptogram quantities of protactinium in geological samples by thermal ionization mass spectrometry. *Anal. Chem.* **66**, 91–108.
- Pyle D. M. (1992) The volume and residence time of magma beneath active volcanoes determined by decay-series disequilibria methods. *Earth Planet. Sci. Lett.* **112**, 61–73.
- Pyle D. M. (1994) Reply to comment by M. Condomines on “The volume and residence time of magma beneath active volcanoes determined by decay-series disequilibria methods.” *Earth Planet. Sci. Lett.* **122**, 257–258.
- Qin Z. (1992) Disequilibrium partial melting model and its implications for trace element fractionations during mantle melting. *Earth Planet. Sci. Lett.* **112**, 75–90.
- Ribe N. M. (1985) The generation and composition of partial melt in the earth's mantle. *Earth Planet. Sci. Lett.* **73**, 361–376.
- Ribe N. M. (1987) Theory of melt segregation—a review. *J. Volcan. Geotherm. Res.* **33**, 241–253.
- Richardson C. and McKenzie D. (1994) Radioactive disequilibria from 2D models of melt generation by plumes and ridges. *Earth Planet. Sci. Lett.* **128**, 425–437.
- Richter F. M. and McKenzie D. (1984) Dynamical models for melt segregation from a deformable matrix. *J. Geol.* **92**, 729–740.
- Rienitz I. and Turekian K. K. (1989) $^{230}\text{Th}/^{238}\text{U}$ and $^{226}\text{Ra}/^{230}\text{Th}$ fractionation in young basaltic glasses from the East Pacific rise. *Earth Planet. Sci. Lett.* **94**, 199–207.
- Rubin K. H. and MacDougall J. D. (1988) ^{226}Ra excesses in mid-ocean ridge basalts and mantle melting. *Nature* **335**, 158–161.
- Rubin K. H. and MacDougall J. D. (1992) Th-Sr isotopic relationships in MORB. *Earth Planet. Sci. Lett.* **114**, 149–157.
- Rubin K., Macdougall J. D., and Perfit M. R. (1994) ^{210}Po - ^{210}Pb dating of recent volcanic eruptions on the sea floor. *Nature* **368**, 841–844.
- Salters V. J. M. and Hart S. R. (1989) The hafnium paradox and the role of garnet in the source of mid-ocean ridge basalts. *Nature* **342**, 420–422.
- Scheirer D. S. and Macdonald K. C. (1993) Variation in cross-sectional area of the axial ridge along the East Pacific Rise: Evidence for the magmatic budget of a fast spreading center. *J. Geophys. Res.* **98**, 22321–22338.
- Sims K. W. W., DePaolo D. J., Murrell M. T., Baldrige W. S., Goldstein S. J., and Clague D. A. (1995) Mechanisms of magma generation beneath Hawaii and mid-ocean ridges: U/Th and Sm/Nd isotopic evidence. *Science* **267**, 508–512.
- Sims K. W. W., Jull M., Kelemen P. (1998) U-series disequilibria and melt transport in the mantle beneath mid-ocean ridges. Presented at American Geophysical Union Meeting, San Francisco CA. Abstract in *Eos: Trans. Am. Geophys. Union* **V22D**.
- Sims K. W. W., DePaolo D. J., Murrell M. T., Baldrige W. S., and Goldstein S. J. (1999) Porosity of the melt zone and variations in solid mantle upwelling rates beneath Hawaii: Inferences from ^{238}U - ^{230}Th - ^{226}Ra and ^{235}U - ^{231}Pa disequilibria. *Geochim. Cosmochim. Acta* **63**, 4119–4138.
- Sinton J. M. and Detrick R. S. (1992) Mid-ocean ridge magma chambers. *J. Geophys. Res.* **97**, 197–216.
- Smith M. C., Perfit M. R., Fornari D. J., Ridley W. I., Edwards M. H., Jurras G. J., Von Damm K. L. (2001) Magmatic processes and segmentation at a fast spreading mid-ocean ridge: Detailed investigation of an axial discontinuity on the East Pacific Rise crest at 9 degrees 37'N. *Geochem. Geophys. Geosys.* **G3**, (paper 2000GC000134).
- Sohn R., Menke W. (in press) Application of maximum likelihood and bootstrap methods to non-linear curve-fit problems in geochemistry. *Geochem. Geophys. Geosys.*
- Spiegelman M. and Elliott T. (1993) Consequences of melt transport for uranium series disequilibrium in young lavas. *Earth Planet. Sci. Lett.* **118**, 1–20.
- Spiegelman M., Kelemen P. B., Ahronov E. (2001) Causes and consequences of flow organization during melt transport; the reaction infiltration instability in compactible media. *J. Geophys. Res.* **B**, Solid Earth Planets **106**, 2, 2061–2077.
- Stolper E., Walker D., Hagar B. H., and Hays J. F. (1981) Melt segregation from partially molten source regions: The importance of melt density and source region size. *J. Geophys. Res.* **86**, 6261–6271.
- Thurber D. (1967) Anomalous $^{234}\text{U}/^{238}\text{U}$ in nature. *J. Geophys. Res.* **67**, 4518.

- Todt W. Cliff R. A. Hanser A. Hofmann A. W. 1996 Evaluation of a 202Pb-205Pb double spike for high-precision lead isotope analysis. In *Earth Processes: Reading the Isotopic Code* (eds. S. R. Hart and A. Basu). *Am. Geophys. Union* **95**, 429–437.
- Toomey D. R., Purdy G. M., Solomon S. C., and Wilcock W. S. D. (1990) The three dimensional seismic velocity structure of the East Pacific Rise near latitude 9°30'N. *Nature* **347**, 639–645.
- Turcotte D. L. (1982) Magma migration. *Ann. Rev. Earth Planet. Sci.* **10**, 397–408.
- Volpe A. M. and Goldstein S. J. (1993) ²²⁶Ra-²³⁰Th disequilibrium in axial and off-axis mid-ocean ridge basalts. *Geochim. Cosmochim. Acta* **57**, 1233–1242.
- Volpe A. M., Olivares J. A., and Murrell M. T. (1991) Determination of radium isotope ratios and abundances in geologic samples by thermal ionization mass spectrometry. *Anal. Chem.* **63**, 913–916.
- Von Damm K. L. 2000 Chemistry of hydrothermal vent fluids from 9–10°N, East Pacific Rise: “Time Zero” the immediate post-eruptive period. *J. Geophys. Res.* **105**, B5, 11203–11222.
- Watson S. and McKenzie D. (1991) Melt generation by plumes: A study of Hawaiian volcanism. *J. Petrol.* **32**, 501–537.
- Weaver J. S. Langmuir C. H. 1990 Calculation of phase equilibrium in mineral-melt systems. *Computers Geosci.* **s16**, 1, 1–19.
- White W. M. (1985) Sources of oceanic basalts: Radioogenic isotopic evidence. *Geology* **13**, 115–118.
- White W. M., Albarède F., and Télouk P. (2000) High-precision analysis of Pb isotope ratios using multi-collector ICP-MS. *Chem. Geol.* **167**, 257–270.
- Williams R. W. and Gill J. B. (1989) Effects of partial melting on the uranium decay series. *Geochim. Cosmochim. Acta* **53**, 1607–1619.
- Wood B. J., Blundy J. D., and Robinson J. A. C. (1999) The role of clinopyroxene in generating U-series disequilibrium during mantle melting. *Geochim. Cosmochim. Acta* **63**, 1613–1620.

Appendix 1a. Major element compositions of 9 to 10°N East Pacific Rise (EPR) axial samples.

Sample	SiO ₂	TiO ₂	Al ₂ O ₃	FeO(total)	MnO	MgO	CaO	Na ₂ O	K ₂ O	P ₂ O ₅	Total
9–10°N EPR											
2359-4	50.39	1.54	14.76	10.06	0.21	7.90	12.01	2.74	0.13	0.19	99.93
2497-1b	50.00	1.52	14.93	10.12	0.19	7.97	12.01	2.77	0.12	0.17	99.79
2359-5	50.57	1.60	14.51	10.45	0.20	7.67	11.75	2.78	0.12	0.22	99.87
2368-4	50.00	1.26	15.58	9.25	0.16	8.55	12.19	2.52	0.07	0.11	99.70
2372-1	49.86	1.31	15.55	9.41	0.16	8.57	12.17	2.56	0.11	0.19	99.89
2392-9	50.04	1.31	15.48	9.38	0.18	8.50	12.15	2.56	0.09	0.13	99.81
2752-6	49.63	1.25	15.71	9.01	0.19	8.94	12.18	2.57	0.11	0.09	99.68
2504-1	50.01	1.30	15.53	9.32	0.17	8.53	12.10	2.54	0.08	0.15	99.73
2351-2	50.01	1.30	15.5	9.41	0.19	8.27	12.3	2.66	0.10		99.77
2746-4	50.10	1.30	15.41	9.37	0.18	8.12	12.03	2.56	0.09	0.14	99.30
2746-3b	49.95	1.17	15.92	8.82	0.17	8.62	11.99	2.44	0.10	0.10	99.26
2370-6	49.90	1.12	15.40	10.00	0.15	8.24	11.60	2.65	0.10	0.09	99.25
2370-1	51.00	1.39	15.30	11.00	0.16	7.54	11.40	2.77	0.12	0.13	100.81
2355-8	50.02	1.56	14.97	9.99	0.21	7.95	11.90	2.83	0.15	0.19	99.77
2356-7	50.58	1.54	14.69	10.03	0.22	8.12	11.83	2.64	0.11	0.19	99.95
2361-6	49.92	1.25	15.4	9.16		8.64	12.3	2.43	0.09	0.14	99.30
2352-2	50.06	1.61	14.60	10.30	0.19	7.80	12.40	2.74	0.11	0.19	100.00
2358-3	50.79	1.67	14.31	10.53	0.23	7.61	11.67	2.78	0.13	0.20	99.92
2358-4	50.66	1.69	14.34	10.62	0.23	7.61	11.68	2.73	0.15	0.19	99.90
2365-3	50.39	1.74	14.31	10.83	0.22	7.55	11.72	2.76	0.12	0.19	99.83
Siqueiros											
2390-5	48.60	2.01	16.00	10.40	0.17	7.01	9.80	3.16	0.63	0.31	98.09
D20-2	48.81	0.96	17.31	7.92	0.1	10.01	12.08	2.35	nd	0.06	99.60
A2384-3	48.95	0.95	17.35	7.98	0.17	10.12	12.09	2.33	nd	0.06	100.00
A2384-6	49.2	0.95	17.14	8.26	0.16	9.57	12.38	2.27	nd	0.05	99.98

Major elements, measured by X-ray fluorescence, in weight percent. Estimated relative errors ~2%, except for Na (5%), P (6%), and K (8%).

Appendix 1b. Rare earth element (REE) compositions of 9 to 10°N East Pacific Rise (EPR) axial samples measured by inductively coupled plasma mass spectrometry (ICP-MS) and isotope dilution thermal ionization mass spectrometry (ID-TIMS).

Sample	La	Ce	Pr	Nd	Sm	Eu	Gd	Tb	Dy	Ho	Er	Yb	Lu
2359-4 ^a	3.4	11.0	1.8	10.0	3.4	1.4	4.9	0.88	5.6	1.2	3.2	3.2	0.52
2359-4 ^c				9.45	3.25								
2359-5 ^b		11.40		10.40	3.59	1.29	5.00		5.84		3.72	3.48	
2359-5 ^c				10.41	3.57								
2368-4 ^a	2.8	9.0	1.6	8.5	2.9	1.2	4.0	0.76	4.7	1.0	2.7	2.7	0.46
2372-1 ^b		9.07		8.24	2.87	1.09	4.04		4.66		2.99	2.79	
2372-1 ^c				8.06	2.80								
2392-9 ^a	3.0	9.7	1.6	9.0	3.0	1.1	4.2	0.75	4.8	1.1	2.8	2.8	0.46
2392-9 ^c				8.24	2.86								
2752-6 ^a	2.9	8.8	1.5	8.2	2.8	1.1	4.0	0.72	4.5	0.96	2.6	2.7	0.43
2752-6 ^c				7.94	2.75								
2504-1 ^a	3.0	9.4	1.6	8.5	3.0	1.2	4.3	0.75	4.8	1.0	2.7	2.8	0.48
2504-1 ^c				8.57	2.98								
2351-2 ^a	2.9	9.3	1.6	8.5	3.0	1.2	4.3	0.78	4.80	1.0	2.8	2.8	0.46
2746-4 ^a	3.1	9.8	1.7	9.3	3.2	1.2	4.5	0.79	5.0	1.1	2.9	3.0	0.50
2746-4 ^c				7.48	2.61								
2746-3b ^a	2.8	9.0	1.5	8.2	2.8	1.1	3.9	0.70	4.5	0.98	2.6	2.7	0.45
2746-3b ^c				7.71	2.67								
2370-6 ^a	2.9	9.2	1.6	8.7	3.0	1.2	4.2	0.75	4.7	1.0	2.6	2.7	0.47
2370-6 ^c				8.07	2.81								
2370-1 ^a	3.5	11	1.9	11	3.6	1.3	5.0	0.92	5.7	1.2	3.5	3.4	0.54
2370-1 ^c				9.95	3.40								
2355-8 ^a	3.4	11.0	1.9	10.0	3.6	1.4	4.9	0.92	5.6	1.2	3.2	3.3	0.53
2355-8 ^b		10.72		9.98	3.44	1.25	4.74		5.66		3.56	3.34	
2355-8 ^c				9.75	3.37								
2356-7 ^a	3.5	11.0	1.9	10.0	3.6	1.4	5.0	0.94	5.8	1.3	3.3	3.4	0.56
2356-7 ^b		10.68		9.80	3.41	1.25	4.86		5.68		3.57	3.35	
2356-7 ^c				9.68	3.35								
2361-6 ^a	2.8	8.9	1.6	8.4	3.0	1.1	4.1	0.76	4.7	1.0	2.7	2.8	0.46
2361-6 ^c				7.87	2.73								
2352-2 ^a	3.7	12.0	2.0	11.0	3.7	1.4	5.20	0.91	5.8	1.3	3.4	3.4	0.59
2352-2 ^b		11.29		10.33	3.55	1.29	4.92		5.80		3.67	3.44	
2352-2 ^c				9.83	3.38								
2358-3 ^a	3.9	12.0	2.1	11.0	3.8	1.5	5.5	0.98	5.9	1.3	3.6	3.5	0.57
2358-3 ^c				10.45	3.59								
2358-4 ^a	3.8	12.0	2.1	11.0	3.8	1.4	5.5	0.97	5.9	1.3	3.5	3.5	0.59
2358-4 ^b		11.90		10.79	3.69	1.34	5.14		6.09		3.84	3.58	
2365-3 ^a	4.0	13.0	2.1	12.0	4.0	1.5	5.7	1.0	6.2	1.4	3.8	3.7	0.62
2365-3 ^c				11.34	3.90								
Siqueiros													
2390-5 ^a	15.0	36.0	4.80	21.0	5.21	1.70	5.90	0.96	5.80	1.20	3.20	3.20	
2390-5 ^c				19.47	5.00								
D20-2 ^a	0.77	3.67		4.31	1.67	0.69	2.56					1.8	
D20-2 ^c				3.87	1.58								
2384-3 ^a	1.11	4.86	0.68	5.26	2.08	0.81	2.83	0.47	2.90	0.64	1.70	2.07	
2384-3 ^c				4.62	1.81								
2384-6 ^a	0.9	3.5	0.72	4.5	1.70	0.69	2.60	0.47	3.00	0.65	1.80	1.70	

^a REE measured by ICP-MS at Geological Survey of Canada; errors 5 to 10% (2σ).

^b REE measured by John Bender by ID-TIMS at the State University of New York Stony Brook; errors for Sm, Nd, and Eu are $\sim 1\%$ (2σ); errors for Ce, Gd, Dy, Er, and Yb are 1 to 2% (2σ).

^c Sm and Nd concentrations measured by ID-TIMS at the University of California, Berkeley; errors $\sim 1\%$ (2σ).

Appendix 1c. Cl, K, Ba, Ni, Nb, Y, Zr, Rb, Sr, and Hf concentrations of 9 to 10° N East Pacific Rise (EPR) axial samples.

Sample	Cl (ppm) ^a	K (ppm) ^a	Ba (ppm) ^b	Ni (ppm) ^c	Nb (ppm) ^c	Y (ppm) ^c	Zr (ppm) ^c	Rb (ppm) ^c	Sr (ppm) ^c	Hf (ppm) ^d
9 to 10°N EPR										
2359-4	32	772	8.82	80	3.3	35.4	101	1.2	122	2.5
2497-1	40	891				36.1	109	0.8	121	
2359-5	79	922	10.91	62	4.5	37.1	112	1.9	125	
2638-4	30	780	7.71	109	2.5	28.4	86	1.4	122	2.2
2372-1	62	710	7.88	110		29.7	88	2.0	125	
2392-9	39	790	8.01	102	2.9	30.0	90	1.8	124	2.2
2752-6	50	807	9.18		2.67	27.5	84	1.0	122	2.0
2504-1	23	737	7.72			30.0	91	1.7	127	2.3
2351-2	40	693	7.66	103	2.3	28.9	89	1.8	123	2.2
2746-4	39	800	8.31			30.3	92	0.9	122	2.3
2746-3b	39	780	7.62			26.7	81	0.9	124	2.0
2370-6	39	780	8.24	110	2.7	29.5	88	2.2	122	2.1
2370-1	117	970	9.85	79	2.4	35.8	107	1.2	123	
2355-8	62	830				2.7	34.8	1.6	124	
2356-7	92	796		77	3.1	34.1	103	2.0	118	2.7
2361-6	50	645	5.98	106	2.6	29.9	86	1.5	118	2.2
2352-2	53	898	9.14	66	2.6	34.6	107	1.7	122	2.8
2358-3	84	942		64	4.3	37.7	116	1.6	123	2.8
2358-4	52	946	10.24	55	2.0	36.3	115	2.0	125	2.9
2365-3	69	947	10.00	53	3.8	38.9	116	0.9	123	3.00
Siqueiros										
2390-5	302	5380	129	107	20.0	35.0	174	12.0	295	4.1
D20-2	9	206	2.6	616		19.0	45		73	
2384-3	20	202	2.22	753	0.48	18.0	45	0.3	58	1.3
2384-6	21	195		340	0.46	18.0	47	0.4	19	1.3

^a Cl and K measured by electron microprobe at University of Tulsa (Michael and Cornell, 1998). Errors for both Cl and K are < 20 ppm (2 σ).

^b Ba measured by isotope dilution inductively coupled plasma mass spectrometry (ICP-MS) at Woods Hole Oceanographic Institution and isotope dilution thermal ionization mass spectrometry at Los Alamos National Laboratory. Uncertainties for both techniques are < 1% (2 σ).

^c Ni, Rh, and Sr measured by X-ray Fluorescence at the University of Florida; errors for Ni are ~ 10%; errors for Rb are < 50%; errors for Nb, Y, and Zr are < 5%; errors for Sr are < 3% (2 σ).

^d Hf concentrations measured by ICP-MS at Canadian Geological Survey; errors are ~ 5% (2 σ).